



ALMA MATER STUDIORUM
UNIVERSITÀ DI BOLOGNA

Università degli Studi di Bologna

DIPARTIMENTO DI SCIENZE DELLA TERRA E DELL'AMBIENTE

Corso di Dottorato di Ricerca in Modellistica Fisica per la Protezione dell'Ambiente

XXIV ciclo

Settore Concorsuale 02/C1

Settore Scientifico-Disciplinare FIS/06

TESI DI DOTTORATO

Detection and Modeling of Boundary Layer Height

Candidato:

Luca Caporaso

Coordinatore:

Ch.mo Prof. Rolando Rizzi

Relatore:

Ch.mo Prof. Rolando Rizzi



ALMA MATER STUDIORUM
UNIVERSITÀ DI BOLOGNA

Università degli Studi di Bologna

DIPARTIMENTO DI SCIENZE DELLA TERRA E DELL'AMBIENTE
Corso di Dottorato di Ricerca in Modellistica Fisica per la Protezione dell'Ambiente
XXIV ciclo
Settore Concorsuale 02/C1
Settore Scientifico-Disciplinare FIS/06

TESI DI DOTTORATO

Detection and Modeling of Boundary Layer Height

Candidato:
Luca Caporaso

Coordinatore:
Ch.mo Prof. Rolando Rizzi

Relatore:
Ch.mo Prof. Rolando Rizzi

Contents

1	Introduction	1
2	BASE:ALFA	5
2.1	Field Phase	5
2.2	Modelling Activities	9
3	Boundary layer height determination	13
3.1	BLH by ceilometer	16
3.2	The Bayesian Selective Method	20
3.2.1	Outline	20
3.2.2	Processing of the lidar signal	24
3.2.3	The physical model for the boundary layer	30
3.2.4	The assimilation procedure	32
3.2.5	Criteria of selection	34
3.3	BSM implementation	34
3.3.1	Initial h estimates: \mathbf{h}_G	36
3.3.2	Error estimation: \mathbf{E} and \mathbf{B} matrices	37
3.3.3	Model background: \mathcal{S}_{bg}	39
3.4	Method assessment	39
3.4.1	Direct validation: comparison to radiosoundings	41
3.4.2	Indirect validation: comparison to black carbon concentration	48
4	Applications	53
4.1	Models and Measurements Comparison	53
4.2	BLH Comparison	59
4.3	Assessment of pollutant concentration	63

5	The Stable Boundary Layer	69
5.1	Introduction	69
5.2	Available dataset	70
5.3	Data analysis	71
6	Conclusions	81
6.1	Acknowledgements	84

Chapter 1

Introduction

The Po valley,¹ in the Northern Italy, is a large plain in a semi-closed basin surrounded by complex orography; the Alps to the North and Apennines to the South-East, and closed to the east by the Adriatic sea. Despite this region (including the flatland of Veneto, Friuli and Romagna) covers only 15% of Italian territory, it hosts 40% of Italian population and produces about 50% of the whole Gross Domestic Product (GDP) of Italy through industry, intensive agriculture and farming. If once, the Po river alluvial plain was called the “granary of Italy” for its farming vocation, nowadays the reconversion to industry makes it the most important contributor to the Made in Italy production.

The described geo-political configuration highly affect this region weather and its air quality. As a flatland basin shielded by mountains, calm wind is very frequent. Strong temperature inversions are often observed near the ground, during the night and in the winter period when the occurrence of a extremely stable boundary layer is common. These conditions produce fog and heavy pollution episodes due to the build-up of pollutants which, emitted at the ground level, remain trapped inside. Indeed, The European Environmental Agency, Technical report No 1/2009 on “Spatial assessment of PM₁₀ and ozone concentrations in Europe (2005)” clearly states that: *“The estimated probability of exceeding the PM₁₀ 36th maximum daily average is considerable in large areas of the eastern European countries and along the entire Po Valley [...].* If during winter the Po valley is oppressed by “smoke and fog”, in the summer it is not unusual the formation of super-cells which

¹The Po valley is named after the Po river which is the major river of Italy cross cutting its Northern regions for approximately 650 km in an east-west direction.

for their intensity resemble tropical storms. The gulf-shaped configuration of the Northern Adriatic sea can be seen as a fuel reservoir providing persistent injection of sea moisture into air masses during cyclogenesis. The land-sea thermal contrasts furnish the ignition for the triggering of convective uplift associated with hail, strong winds and intense precipitations. The consequences are disastrous hydro-geological damages, agricultural loss and serious risks for human safety and transport security.

It is clear that weather forecasting for this area is at the same time relevant and truly challenging due to the inherent low predictability of small scale driven phenomena, and in fact persistent biases in surface parameters are often recorded. Progress now underway to improve the performances of regional scale numerical weather prediction (R-NWP) models in these critic conditions stems from:

- 1) significant improvements in boundary layer and turbulence schemes over the past decade [28, 12], and
- 2) observing initiatives that provide data needed to initialize these models and assess the success of different parametrization [65, e.g.].

Following this main stream of research, this work focuses on a recent experimental program designed and carried out in the middle of the Po Valley. The main aim of the project was the collection of suitable measurements to be employed in R-NWP physical parametrization evaluations and, possibly, improvements. Nevertheless, it was found that the observations collected could also be used to perform impact studies and diagnostic analysis. For example, to test how the skill of R-NWP projects impacts meteorological applications forced by R-NWP.

The Budget of the Atmosphere-Soil Exchange: A Long-term Fluxes Analysis (BASE:ALFA) project was a major ARPA-SIMC sponsored project with the main aim of improving our understanding of the processes that couple the surface to the atmosphere through the boundary layer using observations, numerical simulations, and physical models. The BASE:ALFA project comprises a 4 month lasting experimental phase and a two year period of subsequent modelling studies based on the collected datasets. We looked at two extremes of BL conditions which are usually poorly represented in regional NWP. At the one extreme, we were attempting to improve the forecast of intensive convective activity during the summer season to assess in which measure it will be possible in the future to push the predictability of intense precipitation triggered by strong convective processes. At the other extreme BASE:ALFA was designed to develop new and/or improved parametrizations

able to reproduce extremely stable BL conditions when processes are driven or strongly modulated by buoyant forcing. This should allow better forecast of surface parameters and successful identification of fog episodes.

The thesis begins by briefly describing the region and the instrumentation employed in the field campaign. The dataset collected is described with some details to furnish all relevant information to potential external users. A general description of the intended modeling activities programmed in the frame of the BASE:ALFA project is also reported. After this introductory part, follows a chapter on the new algorithm to define boundary layer height, h , from a lidar scene [18].

The work, then, will focus on a couple of application:

1) How the wrong boundary layer height (BLH) modeling can impact air quality assessment. Air quality models and satellite retrieval algorithm for pollutant concentrations estimations, in fact, uses R-NWP predicted and/or analysed BLH to assess and forecast the concentration of various pollutant (i.e. PM_{10}) and more generally the air quality of a region. These estimations are monitored and used at political level to issue traffic blocking with direct consequences on population lifestyle and productive activities. We will see that the range of variability in the BLH values due to different model choices of boundary layer growth can be relevant but tendentiously not large enough to cause an overstepping of the PM_{10} concentration recommended as maximum amount for health safety accordingly to the European Directive 2008/50/EC.

2) The correct characterisation of very stable boundary layer is of considerable practical importance. The absence of significant mixing allows buildup of high concentrations of contaminants which can be diagnosed directly by the boundary layer height, h . One of the practical consequences of the outlined finding is therefore that formulations of h , which mainly rely on surface turbulent fluxes are inaccurate in very stable conditions. It is then shown as an example that the expression for h suggested by [81, 82] which is a function of surface fluxes and atmospheric stability leads to h estimates in disagreement with the ones obtained by inspecting the mean profiles as in [18].

Chapter 2

BASE:ALFA

2.1 Field Phase

A driving requirement for the BASE:ALFA observational phase design was identified in the need for a very comprehensive set of surface measurements. Since phenomena triggered by processes at the surface-atmosphere interface are especially under observation, not only radiative and turbulent fluxes were a priority but also a whole set of hydrological measurements comprising ground temperature and humidity profiles. Moreover it was underlined by the scientists participating to the campaign that only a long-term datasets could guarantee a vast statistical sampling of cases to make possible sensitivity studies. One of the underlined project aim was the possibility to be able to assess the relative importance played in turn by the ground, the atmosphere and their interaction in the triggering of high impact weather regimes. Considering the large measurement representativity in the Po Valley, it was therefore decided to concentrate all instrumentation available in one meteo base, and to extend the intensive observational period (IOP) so to cover almost four months spanning different seasons. BASE:ALFA was therefore located at SanPietroCapofiume (SPC) in the middle of the Po Valley where a duly operating observing station managed by ARPA-SIMC is in place since 1984. The configuration of the BASE:ALFA instruments appears in figure 2.1 while table 2.1 summarizes their main characteristics and the measured parameters. The whole experimental period covered two IOPs; one during the summer season between the 18th of June 2009 and the 18th of July 2009, one in winter-spring , between the 18th of January and the 18th

of April. During these two phases the whole set of instruments were operating in continuous with time resolution given in table 2.1. The observational data used in this analysis were collected in the framework of the BASE:ALFA project at San Pietro Capofiume (SPC) in the middle of the Italian Po Valley [18].¹ One of the targets of the BASE:ALFA observational experiment was the development of new and/or improved diagnostic formula for h in stable conditions to improve pollutant concentration analysis and forecast for one of the most polluted spot in Europe [25]. Two sets of observations are available; a summer period between June 18 and July 18, 2009 and a winter-spring one spanning January 18 to April 18, 2010. During these two phases a pool of instruments comprising a radiosounding automated station, a ceilometer, an eddy-covariance micrometeorological station, a four-way radiometer, and a full SYNOP surface station were operating in continuous.

For the entire campaign at least one radiosounding (RDS) a day was launched at 00UTC. In addition, at selected dates, this was extended to 4 soundings at synoptic times (00,06,12,18 UTC) to guarantee the characterisation of the full evolution of the boundary layer. The used radiosoundes were model VAISALA RS-90 SGP for the summer campaign and VAISALA RS-92 KL for the winter-spring campaign. These two different models have comparable quality [70]. The first measurement level is at $z_1 \simeq 10\text{m}$, the typical height resolution is 10m and, accordingly with VAISALA instrument specifications, the measurement accuracy is 1m/s for the wind velocity and 0.2K for the temperature. A total of 174 profiles have been recorded of which 47 are classified stable cases being the sensible heat flux at the surface negative.

¹SanPietro Capofiume station is located in the middle of a uniform grassland. The surroundings are farmlands whose typical side size of few hundred meters cultivated with maize, wheat and beetroot

Table 2.1: Summary of the measurements collected during the BASE:ALFA campaign.

Instrument	Variable	Time res	Comments
Radiosonde	Temperature (K)	6h	vertical profile
	Relative humidity (%)	6h	vertical profile
	Wind speed (ms^{-1})	6h	vertical profile
	Wind direction (degrees)	6h	vertical profile
	Virtual potential temperature (K)	6h	vertical profile
Sonic anemometer	Wind velocity (vectorial) ms^{-1}	1h	
	Wind velocity (scalar) (ms^{-1})	1h	
	Wind speed (ms^{-1})	1h	
	Wind direction (degrees)	1h	
	"Sonic" temperature (K)	1h	
	St. dev. of wind direction (ms^{-1})	1h	
	St.dev. of the 3 wind components (ms^{-1})	1h	
	Turbulent kinetic energy (m^2/s^2)	1h	
	St.dev. of temperature (K)	1h	
	Covariances between wind components(-)	1h	
	Covariances between wind components and temperature (-)	1h	
	Friction velocity (ms^{-1})	1h	
	Ratio between anemometer height and Monin-Obukhov length	1h	
	Scale temperature (K)	1h	
Uncorrected turbulent heat flux (Wm^2)	1h	eddy covariance method	
Structure parameters of u,v,w,T	1h		
Infrared Gas Analyzer (IRGA)	Water vapor mass concentration gm^{-3}	1h	
	Carbon dioxide mass concentration (gm^{-3})	1h	
	St.dev. of water vapor mass concentration (mgm^{-3})	1h	
	St.dev. of carbon dioxide mass concentration (mgm^{-3})	1h	
Sonic anemometer + (IRGA)	Vertical flux of water vapor $\text{gm}^{-2} \text{ s}$	1h	eddy covariance method
	Vertical flux of carbon dioxide ($\text{gm}^{-2} \text{ s}$)	1h	eddy covariance method
	Turbulent latent heat flux (Wm^{-2})	1h	eddy covariance method
	Corrected turbulent sensible heat flux (Wm^{-2})	1h	eddy covariance method
Radiometer	Downward short-wave radiation (Wm^2)	600s	Pyranometer: [0.305 to 2.8] μm
	Upward short-wave radiation (Wm^2)	600s	Pyranometer: [0.305 to 2.8] μm
	Downward long-wave radiation (Wm^2)	600s	Pyrgeometer: [5.0 to 50.0] μm
	Upward long-wave radiation (Wm^2)	600s	Pyrgeometer: [5.0 to 50.0] μm
	Net radiation (Wm^2)	600s	
	Sky temperature (K)	600s	
	Ground temperature (K)	600s	
Time-Domain Reflectometer	Soil water content (m^3/m^3)	1h	levels into the ground [10,25,45,70,100,135,180]cm
	Soil temperature (m^3/m^3)	1h	
LiDAR-ceilometer	Range corrected signal (dB)	15m	Derived vertical profile of aerosol concentration
Air quality station	Nitrogen dioxide mass concentration (μgm^{-3})	1h	
	Ozone mass concentration (μgm^{-3})	1h	
	PM ₁₀ mass concentration (μgm^{-3})	24h	Gravimetric

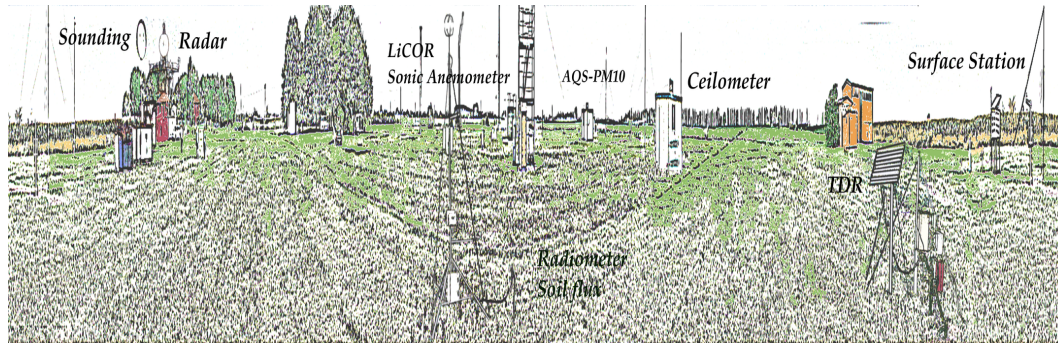


Figure 2.1: Configuration of the BASE:ALFA instruments at the San Pietro Capofiume Meteo Station

In addition to the conventional meteorological measurements including surface and upper air observations, for the BASE:ALFA project, SPC was equipped with additional in-situ and remote instrumentation. The thermodynamical observation of the ground and of its interface with the atmosphere was provided by the combination of a Time-Domain Reflectometer (TDR) and a Meteoflux station comprising a sonic anemometer a LiCOR and a CNR-1 radiometer. The TDR measures soil water content and temperature profiles at 8 unevenly spaced levels below the ground between 10 and 180 cm. The Meteoflux station instead provides through eddy correlation technique [35] surface fluxes of sensible and latent heat, momentum fluxes, in addition to CO_2 and H_2O fluxes. Energy budget both in the shortwave and longwave was also recorded at the soil level by two independent radiometers. Temperature, humidity, zonal and meridional wind and precipitation were recorded in almost continuous mode at 2m and 10 m heights as in a standard synop stations. The remote observation of the boundary layer evolution was provided by a commercial LiDAR-Ceilometer, Vaisala LD-40. This instrument sends 855 nm laser pulses in the atmosphere and records the light backscattered from air molecules and particulate matter. At this wavelength the molecular contribution is small, so the returned range-corrected signal (RCS) is roughly proportional to the aerosol backscatter cross section. In addition to aerosol loads, signal analysis allows to track the BL evolution by using aerosols as markers.

A polarimetric Doppler C-band RADAR was also operating in the field working at a frequency of 5.5 GHz. Reflectivity measurements were acquired

with a repetition cycle of 15 minutes and horizontal resolution of 1 km. Raw data are quality controlled and corrected for clutter, anomalous propagation and beam blocking. Radar acquisitions provide an overview of the convective system crossing the valley and proved to be very useful in the analysis of the evolution of strong convective events during summer.

The whole availability of data for the two IOPs is reported in figure 2.2. The two highlighted periods during the summer and winter campaigns were characterised by clear sky conditions and fair weather. Instability forced the convective growth of the BL height. These periods have therefore been selected for the two case studies discussed in the second part of this article where an explicative application of the BASE:ALFA dataset will be provided.

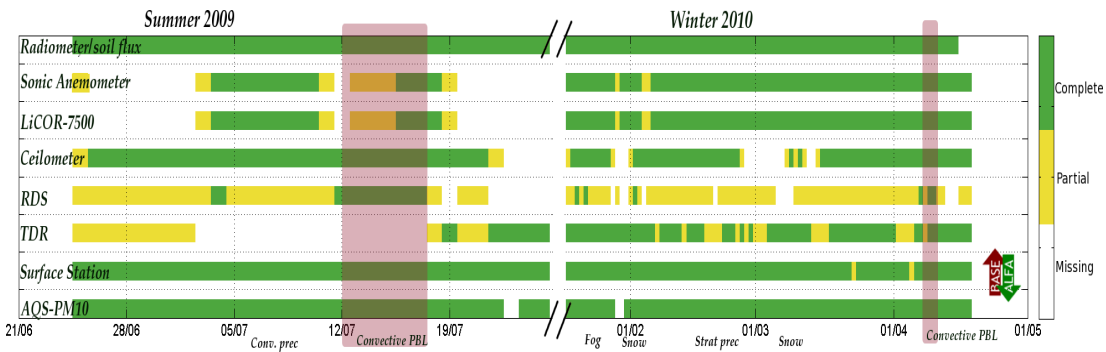


Figure 2.2: Data availability for the two IOPs. The two convective periods which are particularly analysed in this work are underlined.

2.2 Modelling Activities

One of the main objectives of the BASE:ALFA project is to improve surface and boundary layer parametrizations in NWP systems for the benefit of BL driven phenomena forecast e.g. screen level temperature, fog and low level cloudiness, mixing height, convection triggering, and to provide better inputs to air-quality modeling systems. The phenomena taking place in the land-atmosphere interface are very complex, with many feedbacks and non-linearities. It is, therefore, difficult to isolate points of intervention to improve parametrization schemes without an accurate diagnostic of our models weaknesses. For this reason the modelling activities of the BASE:ALFA

project have an high priority; preliminary investigations are concentrated on diagnostic model studies, in a successive phase possible improvements of existing schemes will be explored (e.g. turbulence schemes, SVAT schemes, etc).

The comparison of model simulations to observed fields allow a means to evaluate subgrid-scale parametrizations required by the models while, at the same time, model simulations provide a context for interpreting our measurements. If on the one hand, therefore, we use the collected measurements to validate our forecast models, on the other hand we employ physical model to help the retrieval of of BL variables from remote observations which are then needed to understand the physical process involved.

Although it is important to stress the broader usability of the collected dataset by the numerical weather prediction, the air-quality and remote sensing communities, most simulations in support to the *BASE:ALFA* project are at the moment confined to the use of models which are already in-house to the projects participants. Therefore, weather forecasting experiments mostly use different resolutions and configurations of the R-NWP COSMO model [72] and of its surface schemes, TERRA [67]. Experiments of air quality impact use the chemical transport model CHIMERE [3], while new interfaces between the two systems have been implemented through the creation of post-processing algorithms to derive BL parameters from standard model outputs. The description of the *BASE:ALFA* modelling activities is summarised in in table 2.2.

Table 2.2: Simulations studies conducted in support of BASE:ALFA.

Study	Simulations	Expected outcome
Atmospheric boundary layer in the Po Valley in convective situation	LES type of simulations from COSMO mesoscale model at different spatial and temporal resolution	Assessment and tuning of convective precipitation forecast capability
Atmospheric boundary layer in the Po Valley in stable to very stable situation	Verification of turbulence closure schemes and development of new parametrizations in very stable conditions	Better forecast of surface parameters and successful identification of fog episodes
Definition and verification of schemes for boundary layer height (BLH) determination in different stability conditions	Implementation of post-processing methods for BLH determination from standard model output	Better characterization of pollutant dispersion for air-quality assessment
Optimization of SVAT schemes	Simulations forced by the observed dataset	Tuning and improvements of parametrizations
BLH estimation from LiDAR measurements	Combination of standard wavelet LiDAR signal processing technique with a physical model of boundary layer evolution (bulk model) employing a Bayesian statistical inference procedure	Corrected estimates of BLH from LiDAR signal
PM ₁₀ retrieval from satellite Aerosol Optical Depth (AOD) products	Application of several BLH models to optimise scale correctly scale AOD	Correct estimates of PM ₁₀ concentration over vast areas

Chapter 3

Boundary layer height determination

Stull [73] defines the planetary boundary layer as the region where air masses are strongly influenced by surface processes and which interacts through exchange processes with air masses originating from above. Being strongly coupled with the ground, this thin layer usually responds to changes in surface forcing on time scales of the order of hours. Turbulence is produced by shear and heat flux, and characterises the layer, leading to rapid fluctuations in quantities such as flow velocity, temperature, moisture etc. and to intense vertical mixing.

Being interested in the evaluation and modelling of exchange processes one key quantity to be evaluated is the boundary layer height (BLH), both from observed variables [68] and from models [77]. From the point of view of numerical weather prediction systems, BLH can be considered as a diagnostic variable to highlight problems in the energy and momentum exchange between the surface and the atmosphere. Large uncertainties in the estimation of this parameter can mean bad forecast capability for BL driven atmospheric phenomena, such as fog, mist or surface triggered convection and/or poor surface forecast scores for variables such as 2m temperature or humidity. From the point of view of chemical transport models BLH is an input parameter characterising the vertical dilution capability of the atmosphere.

Since the main application of BLH estimate attains pollution from ground level sources, in the following we will discuss in fact how to estimate the height reached by a passive tracer released near the ground in equilibrium

conditions. In the case studies presented, BLH is modelled using the outputs of the limited area model COSMO or derived by indirect observations, such as LiDAR observations or radiosounding profiling. It has to be noted that BLH is neither a standard output of the COSMO model nor a directly measurable quantity; several are the approaches that can be followed to estimate this quantity. Possible methods (hereinafter indicated as bulk Ri, gradient Ri or TKE methods) are based on the investigation of the turbulence properties of the atmosphere with height. The BLH is defined, then, as the level at which turbulence drops (or it is supposed to drop) below a critical value. Three methods largely used in the literature to calculate BLH from R-NWP model outputs have been considered here. For all the methods, the distinction between stable and unstable conditions is made on the basis of the sign of the sensible heat flux, H_s , estimated at the surface.

The *gradient Richardson number* method defines the BLH as the elevation of the lowest level of the model where the gradient Richardson number, R_g , exceeds a critical value, R_g^{crit} . The *gradient Richardson number*

$$R_g(z) = \frac{g}{\theta_v(z_0)} \frac{\partial \theta_v}{\partial z} \backslash \left[\left(\frac{\partial u}{\partial z} \right)^2 + \left(\frac{\partial v}{\partial z} \right)^2 \right] \quad (3.1)$$

can be defined for each atmospheric layer as the ratio between the turbulence inhibition for buoyancy and the turbulence production due to wind shear. Conceptually, therefore, an $R_g^{crit} < 1$ tries to identify a vertical level where the eddies production due to surface drag is compensated by the thermal stratification of the atmosphere. The *bulk Richardson number*

$$R_b(z) = \frac{gz}{\theta_v(z_0)} \frac{\theta_v(z) - \theta_v(z_0)}{u(z)^2 + v(z)^2} \quad (3.2)$$

method is a discretization of the latter method where, again, BLH is defined as the elevation of the lowest level of the model where R_b , exceeds a critical value R_b^{crit} . Note that conceptually the two methods are equivalent, but the substitution of the differential gradients to finite differences can lead to a different choice of R_b^{crit} with respect to R_g^{crit} [68]. The last approach implemented is the *turbulent kinetic energy - TKE* method

$$TKE = \frac{1}{2} \left(\overline{(u'_1)^2} + \overline{(u'_2)^2} + \overline{(u'_3)^2} \right) \quad (3.3)$$

where BLH is defined as the elevation of the lowest level of the model where the turbulent kinetic energy drops under a critical value TKE^{crit} .

This value is determined as $TKE^c = TKE^{max} * r$ where TKE^{max} is the maximum value of TKE in the boundary layer, and r is the critical ratio. The idea here is to find the vertical level at which the transmission of kinetic energy, which is proportional to the variances of the wind components, from the atmosphere to the air parcels is smaller than a certain amount. The important difference that has to be noted with respect to the other two approaches is that the TKE method relies on the model prediction of the second moment of the velocity distribution (i.e. the variances of wind components (u^2, v^2, w^2)) which is likely to be largely less accurate than the first moment used in the previous two methods.

Benchmark estimations are also needed for comparison and are obtained using two indirect measurements; vertical profiles from radiosounding and LiDAR processed backscattering signal. Under unstable conditions, BLH evaluation from radiosounding profiles is based on the analysis of the virtual potential temperature profile [33]. It follows the idea that an air parcel leaving the ground with a given surface virtual potential temperature can reach the height where atmosphere has the same virtual potential temperature, which is then taken as BLH. On the contrary, in a stable BL the empirical inspection of the potential temperature profile leads to evaluate the height at which there is the transition from stable to neutral condition, possibly matching with the height of maximum wind.

“Direct” BLH estimation from the LiDAR signal is finally obtained by applying the Bayesian algorithm of [18] to the backscattered LiDAR signal as already explained. Table 3.1 summarises the methods implemented and used in the following sensitivity studies.

It has to be re-called that another family of methods exist which use mainly the surface fluxes (plus some overall information about atmospheric stability above the BL), and can be applied both to model outputs and to eddy correlation measurements [80, 82]. These approaches are nevertheless applicable to calculate the BLH in stable to very stable conditions and are therefore not considered in this particular application presented here which focusses on the daily growth of convective BL conditions but for some specific analysis of stable BL using the BASE:ALFA dataset the interested reader can refer to [44].

3.1 BLH by ceilometer

The present availability of low-cost commercial ceilometers (low-power automated laser-radar or lidars) provides an opportunity to widely employ these instruments to furnish continuous observation/estimates of the boundary layer (BL) evolution using the detected aerosol stratification. This capability may serve the scope of both air-quality model initialisation and numerical weather prediction system evaluation.

To analyze the return signal in laser remote sensing means to find solutions for the equation which relates the characteristics of the received and emitted signal, and the propagation medium. This equation is described by the so-called lidar equation, which in the simplest case of elastic backscattering lidar can be written as follows :

$$P(\lambda, R) = C [\beta_{mol}(\lambda, R) + \beta_{aer}(\lambda, R)] e^{[-2 \int_0^R \alpha_{mol}(\lambda, R) + \alpha_{aer}(\lambda, R)] dR} \frac{1}{R^2} + B \quad (3.4)$$

where:

P is the lidar backscatter signal

λ is the wavelength of sounding radiation

R is the laser path from the transmitter

C is the system constant and it is equal to $\frac{c}{2} E_0 A(r)$ where c is the speed of light, E_0 is the laser energy emission and $A(r)$ is the telescope area

β_{mol} is the molecular backscatter coefficient

β_{aer} is the aerosol backscatter coefficient

α_{mol} is the molecular extinction coefficient

α_{aer} is the aerosol extinction coefficient

B is the background noise

After the background noise has been subtracted from the backscattered signal, this is range-corrected (the range-corrected signal will be indicated with $S \times R^2$).

$$S \times R^2 = C [\beta_{mol}(\lambda, R) + \beta_{aer}(\lambda, R)] e^{[-2 \int_0^R \alpha_{mol}(\lambda, R) + \alpha_{aer}(\lambda, R)] dR} \quad (3.5)$$

Aerosol Lidar measurements at one wavelength can deliver aerosol backscatter profiles using inversion (two unknowns appear in the single-wavelength

elastic lidar equation: the aerosol extinction α_{aer} and the aerosol backscatter β_{aer}). The molecular contributions (β_{mol} and α_{mol}) of the backscatter and respectively extinction coefficients can be computed from pressure and temperature profiles using the standard atmosphere model, but the aerosols contributions must be both derived by inverting the lidar equation (e.g. by considering a constant profile of lidar ratio [39]).

For ceilometers operating in the near infrared the intensity of the backscattered signal is, to a first approximation, proportional to the aerosol extinction cross section. The hypothesis is made that incoherent and elastic scattering by randomly distributed aerosol and molecules takes place at the ceilometer functioning frequency. Unfortunately, the backscattered signal undergoes an important extinction while propagating back to the receiver which results in a partial loss of proportionality to the aerosol backscatter coefficient. In fact for ceilometers, and in all lidars where the signal cannot be calibrated against the pure molecular echo, a measure of the error arising from the signal extinction can be obtained from an analysis of the expected atmospheric transmission (T_a).

For ceilometers, which operate typically in the wavelength range 800 – 1100 nm, and for ordinary aerosol conditions (with optical thickness of 0.1 at 870 nm), the associated T_a is 0.82 (the molecular optical thickness can be neglected as it is about 0.016). This leads to a maximum underestimation of the aerosol backscatter coefficient of about 20% at the top of the aerosol layer¹

If aerosols are present, ceilometers can thus be used to track the boundary layer evolution. Due to this capability, the COST(European Cooperation in Science and Technology) Action ES0702² suggested that given a sufficient aerosol lidar/ceilometer network, lidar data could play a role in enriching Numerical Weather Prediction (NWP) data assimilation systems and encouraged the simultaneous definition of more sophisticated data processing procedures to furnish reliable retrievals of the boundary layer depth, h . Some successful assimilations of lidar derived information have already been demonstrated in the work of [36, 37, 79].

Several problems can arise when marker-based methods are employed to

¹ T_a is described by a monotonically decreasing function that modulates the backscatter signal. In practice the inflection points, that we are looking for the determination of boundary layer height, are not influenced by this.

²European Ground-Based Observations of Essential Variables or Climate and Operational Meteorology (EG-CLIMET)

estimate BL heights from ceilometer returns. First of all, the presence of aerosols (the marker) is a main requirement. Aerosols above the instrument may still be advected or removed by wind, which would make the simple strategy of analysing one single vertical lidar signal unreliable. Only under the strict condition of horizontal homogeneity and low wind speed are aerosols usable as markers of BL dynamics. It will be shown, however, how this shortcoming can be mitigated by the use of consecutive profiles. Other detection problems arise from rain, clouds or fog. Hydro-meteors quickly extinguish the ceilometer signal and in general no information can be retrieved above these. In these cases, only data below the cloud layer can be processed, while, in case of fog, no retrieval is possible at all. Finally, multiple aerosol layers can be present in the atmosphere; especially if vertical mixing is weak. Aged aerosols may remain suspended in a persistent residual layer, which is detected as a stratification even if it is not significantly connected to the actual boundary layer height.

In recent years algorithms have been proposed to retrieve h from the elastic backscatter signal of lidars. In the simplest approach the signal is analysed on each independent profile (1D methods) by searching for the strongest signal gradients along the vertical dimension (for this reason these methods are usually referred to as “gradient methods” [23, 26]. Other approaches use a simple threshold on the backscatter ratio or backscatter coefficient [52], or a more powerful analysis of the temporal variance of the signal [32]. Research lidars are obviously more powerful than ceilometers and can provide data with better signal-to-noise ratio and higher spatial and temporal resolution. This also allows the PBL height determination by analysis of the temporal variance of the signal. As an alternative, the retrieval of water vapour by Raman or DIAL (Differential Absorption Lidar) techniques or the use of temperature lidar may be employed as in [62]. However, as reported by [32], analysis of aerosol backscatter with respect to water vapour backscatter provide very similar results. It should also be noticed that the variance technique has the weakness that in the case of atmospheric stability, very common at nighttime, no turbulence can induce fluctuations in water vapour profiles or aerosol backscatter coefficient, hence no strong variance at the top of the layer is expected in lidar signal. Studies employing the temporal variance of lidar $S \times R^2$ signal or water vapour mixing ratio are thus mostly limited to convective regimes [32, 41, 59, 1]. Under stable conditions, it is difficult to define the PBL height with confidence [49], and its determination is still problematic for lidar/ceilometers. The assisted analysis of ceilometer

records presented in this paper provides an increased accuracy if automated detection of BL height is required.

Gradient methods are better suited for the PBL height determination with low-power ceilometers than variance methods because the requirements regarding temporal resolution and signal-to-noise ratio of the data are less stringent. Technically the processing is performed either by direct numerical calculation, finding the relative minima of the first derivative of the range-corrected signal, or by means of the Wavelet Covariance Technique (WCT). The latter, initially employed by [21, 78, 38, 15, 66, 74, 9, 8, 16, 5] and more recently by [54, 51, 50], consists in the convolution of the vertical signal with a step function, which is able to detect local discontinuities in the back-scatter profile. For each column these signal processing techniques identify multiple points along the vertical. An assumption needs then to be made to select which inflection point actually marks the PBL h . The strongest discontinuity or the lower one are just two examples of possible criterion if the aid of a subjective inspection to the Ceilometer scene is not available.

There exists another class of methods which, in the retrieval process, takes into account not only the altitude-dependent intensity of the lidar signal but also its temporal variation. For this reason, they are referred to as two-dimensional (2D) techniques. The lidar signal scene is processed as an image and edge detection is performed, as for example by applying the Roberts filter, or the Canny algorithm [6, 20, 64]. Though the idea of introducing the information on the temporal variability of the instrument signal is clearly appealing, such image processing approach is possibly not the most suitable one for very noisy signals, $S \times R^2$, as in the case of the lidar/ceilometers. Signal discontinuities are often of the same order of magnitude of the noise and this makes the edge detection process quite problematic.

To overcome these limitations we propose a new method which applies a time-dependent criterion of selection between the various stratifications as detected by either a standard gradient or wavelet 1D approach. The method is statistically based and is designed to automatically select in Bayesian terms the most likely h between all the detected stratifications. This is accomplished by merging information from the marked vertical lidar signal processing output with a description of the BL diurnal evolution as predicted by a physical model. The two items of information are combined in an *optimal* way using a Bayesian data assimilation technique [14]. Firstly a model prediction which best fits the initial lidar estimates of boundary layer heights is retrieved. This "trajectory" which describes the actual PBL evolution is

then used to discriminate between realistic and unrealistic lidar inflection points and ‘regularise’ experimental values. Since the assimilation procedure is used as a first step to then *select* which of the detected points is most likely representative of the boundary layer height, we will refer to the new method as the Bayesian Selective Method (BSM). It has to be stressed that while the BSM always provides a final h estimation, its accuracy strongly relies on the capability of the lidar columnar signal processing to mark meaningful atmospheric stratifications. Therefore an extensive testing of the new approach is presented by using the dataset collected in the framework of the BASE:ALFA project,³ which collected a whole set of surface measurements during two intensive observation periods (IOPs) in summer 2009 and in winter-spring 2010 at San Pietro Capofiume in the middle of the Italian Po Valley.

A detailed description of the BSM is given in section 3.2. We will discuss the basic theory behind the retrieval method and solutions for a practical implementation. The validation of the BSM and its performance, also compared to other selection techniques, are discussed in the following sections.

3.2 The Bayesian Selective Method

3.2.1 Outline

The Bayesian Selective Method is a time dependent algorithm to define boundary layer height, h , from a lidar scene. It identifies which lidar signal discontinuity, from the ones detected by standard wavelet or gradient analysis, can be considered, in statistical sense, the best retrieval of h . In contrast to standard 1D approaches the selection criterion is not prescribed a priori, for example on the basis of empirical thresholds set on $d(S \times R^2)/dz$. Instead it is re-validated for each single scene using the prediction of a physical model which diagnoses the daily evolution of the boundary layer. The procedure works on a temporal window of one day and follows several steps which are schematised in figure 3.1.

Initially, the acquired lidar scene is processed. For each independent column profile a number, n_G , of vertical stratifications are identified where discontinuities in the lidar back-scattering signal occur. This can be done

³Information and data from the “The Budget of the Atmosphere-Soil Exchange: A Long-term Fluxes Analysis (BASE:ALFA)” project are available at <http://www.smr.arpa.emr.it/basealfa/>

either by direct numerical differentiation or by a wavelet-based technique. Both approaches allow for determination of the strength and sign of inflections, and for determination of multiple layers. The wavelet analysis, being based on an integral rather than a differential method, is more robust and less sensitive to noise, also due to its multi-scale approach. Conversely, the wavelet transform suffers of a large blind zone, which is half of its maximum extension, as already observed in [5]. This makes it impossible to detect low altitude inflection points, which are instead very common at nighttime, as it can be seen in figure 3.1, for example. The gradient method does not suffer from this problem, and can be successfully used in case of non noisy signals, as of low altitude echoes. Our analysis has been performed employing both the direct numerical differentiation and the WCT.

Figure 3.1 shows a lidar-Ceilometer acquisition for an example day and in panel A the edges of the wavelet analysis detected stratifications are signed. An automated algorithm should then *select* which of these points marks the BL height. The requirement for automation of the lidar scene processing (i.e. without the aid of an experienced operator) is emphasized, therefore, an a-priori criterion of selection should be set. The highest values between the convolution of the $S \times R^2$ and the wavelet function or the sharpest stratification, or the lowest stratification border, i.e. the first signal discontinuity identified by the lidar are possible choices. In figure 3.1 panel B, h_{G1w} retrieved by selecting the strongest convolution signal is depicted. It is evident that the vertical spread of the detected stratifications at a given time is quite relevant. The criterion of selection based on defining a threshold on the $S \times R^2$ -wavelet convolution function is often not effective. During nighttime, for example, $G1_w$ picks up stratifications which are due to residual layers and which are not effectively related to the BL evolution. An experienced analyser of this specific lidar scene would discard these points as possible h . Similarly, a good automated selection criterion should be able to discriminate discontinuities due to physical process in the BL from the ones due to spurious signals. Nevertheless this is difficult to achieve if the retrieval is performed independently on single vertical columns not taking into account knowledge from the neighbouring columns.

In the BSM the time-information is exploited by employing a physical model of the BL evolution. The so-called *bulk* or *slab* model, \mathcal{S} [4, 7, 75] for its ease of implementation has been chosen at this purpose. Effectively the BSM method is independent of the choice of the underlying BL model and other, more complex, models could be easily substituted. A climatological

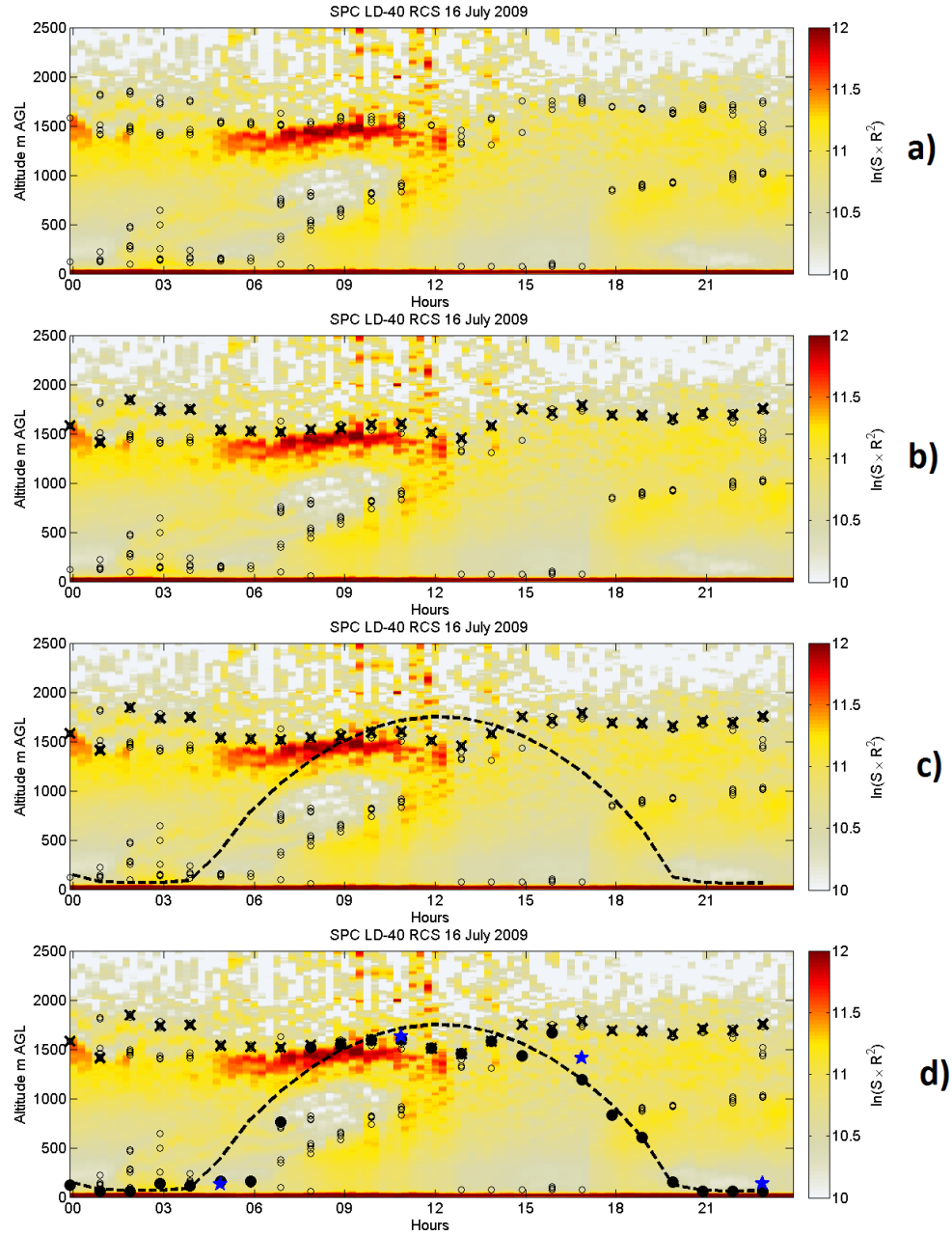


Figure 3.1: Schematic explanation of the Bayesian Selective Method. The procedure works on a temporal window of one day and follows several steps. The lidar signal is processed on each independent column to identify discontinuities (empty circles, in panel A). Among them, BL heights are diagnosed (crosses in panel B). These are then used in combination to a physical model, \mathcal{S} , to describe the daily evolution of the BL. The curve $h_{\mathcal{S}(an)}$ (dashed line, panel C) is the solution of the physical model \mathcal{S} which optimally fits the dataset. $h_{\mathcal{S}(an)}$ is then used to chose which, among *all* the detected stratifications, is the best, in statistical sense, BL height. The filled circles in panel D mark the h_{BSM} estimations. The stars are the available h estimates from radiosoundings.

solution of the model \mathcal{S} provides the background (or “first guess”) hypothesis of a possible BL evolution for the day. Then an analysed model trajectory is found that minimises, in statistical sense, the distance between the background prediction and the actual BL heights (either provided by $\mathbf{h}_{\mathcal{G}1}$ ⁴, or any other 1D estimation). Figure 3.1 panel C shows the \mathcal{S} solution which best fits the given $\mathbf{h}_{\mathcal{G}1_w}$ data vector. The analysis vector, $\mathbf{h}_{\mathcal{S}(an)}$, is a smooth solution of the physical model, \mathcal{S} , and contains height estimations which do not necessary correspond to local lidar signal discontinuities. The trajectory can nevertheless be used as a dynamical criterion of selection between all lidar stratification edges by using, for example, the proximity to the retrieved $\mathbf{h}_{\mathcal{S}(an)}$ values as a metric. After the application of this selection the BSM retrieved h are visualised in figure 3.1 panel D. Subjective estimations of h from high resolution radiosounding profiles are also marked for reference.

If $\mathbf{h}_{\mathcal{G}}$ indicates the vector with the m daily BL height estimates as derived applying a threshold to the wavelet/gradient analysis of the instrument signal, and $\mathbf{h}_{\mathcal{S}}$ is the equivalent vector containing the model estimations, then an optimal combination which is the analysed *solution* of the model \mathcal{S} ($\mathbf{h}_{\mathcal{S}(an)}$) can be obtained through the minimisation of a cost function J [46]:

$$\begin{aligned} \mathbf{h}_{\mathcal{S}(an)} : \min(J(\mathbf{h}_{\mathcal{S}})) = & \\ & + \frac{1}{2} (\mathbf{h}_{\mathcal{S}} - \mathbf{h}_{\mathcal{S}(bg)})^T \mathbf{B}^{-1} (\mathbf{h}_{\mathcal{S}} - \mathbf{h}_{\mathcal{S}(bg)}) + \\ & \frac{1}{2} (\mathbf{h}_{\mathcal{S}} - \mathbf{h}_{\mathcal{G}})^T \mathbf{E}^{-1} (\mathbf{h}_{\mathcal{S}} - \mathbf{h}_{\mathcal{G}}) \end{aligned} \quad (3.6)$$

The solution, $\mathbf{h}_{\mathcal{S}(an)}$, therefore represents a compromise between two sources of information: the background evolution of the BL height as predicted by the model climatology, $\mathbf{h}_{\mathcal{S}(bg)}$, and the lidar initial estimations of BL heights, $\mathbf{h}_{\mathcal{G}}$. The error covariance matrices \mathbf{B}^{-1} and \mathbf{E}^{-1} weigh the credibility of the model assumptions and the experimental data, respectively.

In the following each step of the outlined method will be discussed in detail.

⁴As a general notation rule bold variables indicate vectors or matrices. Here the variable $\mathbf{h}_{\mathcal{G}1} = (h_{t=1}, \dots, h_{t=m})$ indicates therefore the vector with the m daily BL height estimates as derived by the wavelet or the gradient analysis. Instead $h_{\mathcal{G}1}$ indicates one single element of the vector

3.2.2 Processing of the lidar signal

The identification of atmospheric stratifications from the lidar signal is the first step of the BSM approach. Since the choice of how this is done is not, strictly speaking, essential to the BSM, two different signal processings have been applied to the lidar-Ceilometer used in this study; the so called gradient method and wavelet approach. The data used have been collected at San Pietro Capofiume during the BASE:ALFA campaign by an automated ceilometer Vaisala LD-40. This system operates at 855 nm, with a pulse repetition rate of about 5 kHz, a vertical resolution of 7.5 m and a native temporal resolution of 15 s. Following [23, 26] the position of inflection points in the back-scattered signal are identified. However, the signal is time-averaged over 15 minutes to improve its signal-to-noise ratio. Subsequently, it is background-subtracted and corrected by the instrument overlapping function. Infact, the well-known lidar equation (3.4), assumes that the volume of space containing the transmitted pulse is completely imaged onto the detector

$$A(t) = A(r) \quad (3.7)$$

where $A(t)$ is the effective receiver area and $A(r)$ is the telescope area. Nevertheless, as a result of the typical separation distance between the biaxial lidar transmitter and receiver (order of centimeters) and the narrow beam width, the irradiated volume at ranges below a certain altitude (altitude of full overlap) are detected incompletely, and the signal at that near range is dominated by this effect.

$$A(t) = O(R)A(r) \quad (3.8)$$

where $O(R)$ is the overlap function and it is the ratio between the energy coming from an object set at range R and the energy really detected. The function $O(R)$ is null at ground and, if the exit pupil is sufficiently large, tends to 1 as $\lim_{R \rightarrow \infty}$. Even the coaxial systems can be affected by incomplete overlap, when the optical axes of the transmitter and receiver are misaligned. Thus, the overlap function provides a measure of the amount of backscattered power coming from a distance z , which is collected by the receiver telescope and imaged onto the detector [29]. Since the 70s, literature has reported different methods to determine the overlap function that can be grouped into two different categories: theoretical and experimental ap-

proaches. The theoretical computations are based on the specifications and configuration of optical elements as the laser beam cross section, the beam direction, beam divergence and the telescope optics. The inconvenient of such approaches is that they require a good knowledge of these specifications to derive an overlap function with enough accuracy. In addition, the parallelism between the laser beam and the telescope optical axis is necessary, which is quite difficult to ensure, especially for mobile lidars. Consequently, an experimental determination of the overlap function is required to derive an accurate correction for real lidar data⁵

Finally, a dilution factor $1/R^2$ is applied, leading to the Range-Corrected Signal ($S \times R^2$).

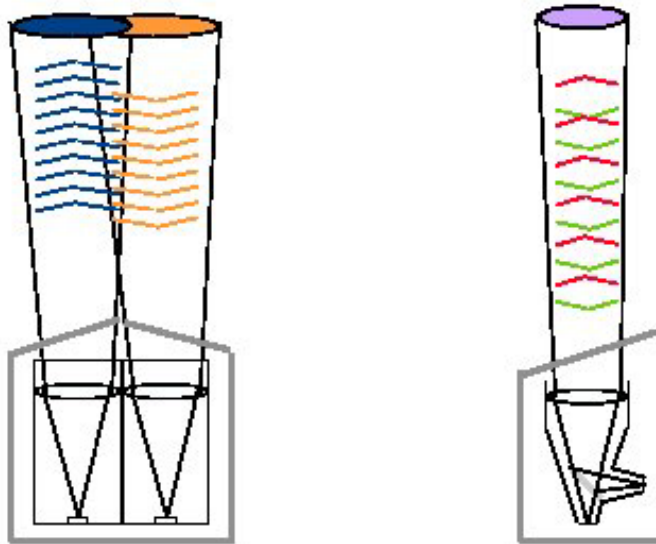


Figure 3.2: Left: bi-axial (e.g. LD-40) versus right: co-axial (e.g. CT25K, CL31) ceilometer design (from [55])

⁵The LD-40 is a bi-axial system, hence the beams of the transmitter and receiver do not overlap completely in the lowest 1125 m. This is a disadvantage with respect to a co-axial (i.e. single lens) system, like e.g. the CT25K ceilometer. Up to 60 m the overlap of the LD-40 is zero, therefore it is not possible to extract any backscatter information from gates below this level. Any received signal below 60 m results from multiple scattering. Between 60 and 1125 m, the overlap increases to 1. The backscatter signal measured in this range has to be corrected for the incomplete overlap between transmit and receiver beam [55]

Due to the limited aerosol signal-to-noise ratio of the ceilometer, the direct numerical differentiation may introduce a number of spurious minima when the first derivative of the signal is scanned for inflection points. To reduce such effects, the signal is spatially averaged with a variable size window (from 50 m near ground to 200 m above 3 km). The $S \times R^2$ inflection points, which are tracers of atmospheric stratifications, are searched employing both the derivative of the signal calculated by finite differentiation (gradient method)

$$G(R) = \frac{d}{dR} \log(S \times R^2) > \text{threshold} \quad (3.9)$$

and the WCT, which consists of the convolution of the signal and a wavelet function

$$h\left(\frac{z-b}{a}\right) = \begin{cases} 1 & : b - a/2 \leq z < b \\ -1 & : b < z \leq b + a/2 \\ 0 & : \text{elsewhere} \end{cases} \quad (3.10)$$

where z denotes the height for our application. The dilation (width) of the wavelet is described by a , while the translation (location at which the wavelet is centered) is given by b 3.3.

The localised transform delivers the wavelet power spectrum coefficients $W_B(a, b)$, calculated as:

$$W_b(a, b) = a^{-1} \int_{z_0}^z (S \times R^2) h\left(\frac{z-b}{a}\right) dz \quad (3.11)$$

which can be interpreted as the convolution of the range corrected signal and the Haar wavelet function, integrated between the bottom and top altitudes of $S \times R^2$ [31, 54, 5] The Wavelet algorithm is applied to the 15 minute averaged range and overlap corrected backscatter profile $S \times R^2$ within a vertical domain of 60–3000 m. For each column these signal processing techniques identify multiple points along the vertical. The parameter a^{-1} denotes the corresponding normalisation factor. Positive values of $W_B(a, b)$ coincide with levels at which the backscatter profile is positively correlated with the Haar function, i.e. the backscatter signal shows a strong decrease with increasing height. They are typically observed at the top of an aerosol layer. The highest values of $W_B(a, b)$ are generally found at height levels for which

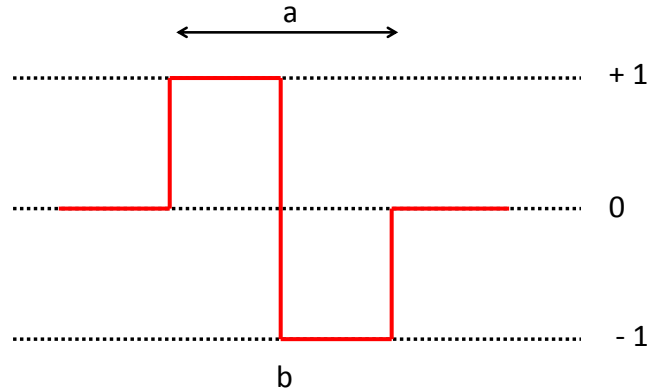


Figure 3.3: A representation of the Haar wavelet function, with dilation a and translation b . (from [31])

the strong decrease in backscatter is vertically spread over the size of the dilation under consideration. Vice versa, negative values of $W_B(a, b)$ indicate an anticorrelation of the backscatter profile with the Haar function for the corresponding dilation 3.2.2. This means that a strong increase in backscatter is observed at the corresponding height, which occurs most likely around cloud base or at the lower boundary of an aerosol layer. The top of the first layer, MLH, is detected at the lowest level at which the scale averaged power spectrum $W_B(b)$ shows a local maximum, exceeding a threshold value of 0.1. This threshold value is empirically chosen, based on the analysis of several cases both with well and less clearly pronounced mixing layer tops.

This wavelet is characterised by the size of its non null part (usually referred to as dilation a), which determines the scale of the features that can be revealed by the WCT. The dilation of the algorithm employed spans from a minimum of 90 to a maximum of 360 m. As already mentioned, this multi-scale approach does not allow the retrieval of inflections laying below the half of the maximum dilation. This limitation can be overcome retaining the direct numerical derivative of the signal where the lidar signal is strong and

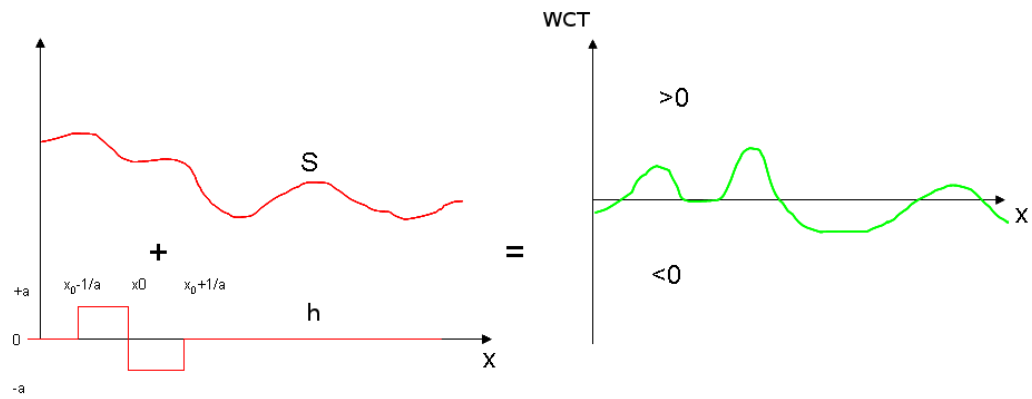


Figure 3.4: The Haar wavelet function is defined in the same space of the starting function and it depends on the shape and size of h (allows multiscale analysis). It is based on integral rather than numerical differentiation (good for noisy signals). The peaks reveal the inflection points. The main hindrance is that the step function has a finite size, so that the search for inflection points has dead zones at the boundaries. These zones are large the half of the wavelet size. Anyway, a threshold is required to determine the lowest inflection point. We chose the first maximum above the threshold exceeding. (F.Angelini personal communication)

the noise is not a significant problem. In fact, thanks to the shape of the Haar function, the maxima of the WCT can be compared to the inflection points of the signal which are relative to minima of the first derivative. Another problem arises when very low layers are investigated. An accurate overlap function of the instrument must be considered to avoid artifacts where such correction is strong. The ceilometer data used in this campaign have been corrected for the overlap with a suitable transfer function 3.5, whose shape is very similar to those provided by Vaisala for these instruments and shown in [31]. The overlap-corrected signal is then reliable for layer detection above 60 m.

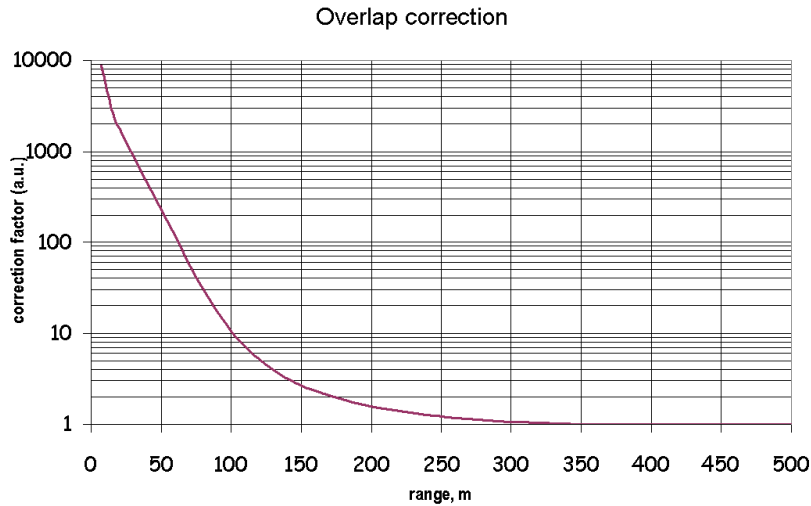


Figure 3.5: The overlap function used for the VAISALA LD-40

A further analysis is finally performed to calculate errors associated to each layer, which are also needed to construct the error covariance matrix \mathbf{E} of equation 3.6. The hypothesis is made that the error associated with each layer height can be related to its altitude and/or time variability. All the WCT maxima and the minima of the $S \times R^2$ gradient are then considered within their respective domains. The set of inflection points from three contiguous profiles (45 minutes of measurements) are grouped into a single profile and sorted by height. Single layers are then identified by checking the distance between each pair of contiguous points: a layer is made by all points whose relative distance is smaller than a threshold value. This threshold ranges from

60 to 120 m according to the season, since the typical scales of the winter boundary layer is approximately half that of the summer one. Finally, a mean height and the standard deviation are computed for each layer containing more than one point. This clustering procedure allows both to exclude some noise-induced inflection points and to associate an error bar to each of the layers resulting from this data analysis. These errors are then also needed to construct the error covariance matrix \mathbf{E} of equation (3.6). A maximum number of seven vertical layers (inflection points) are finally stored each hour for the following BSM to utilize.

3.2.3 The physical model for the boundary layer

The idealised boundary-layer model used in the practical implementation of the BSM is the so-called *bulk* or *slab* model, \mathcal{S} [73]. The main assumption of the slab model is that the potential temperature can be considered constant within the boundary layer while a topped temperature inversion confines the lower ‘well-mixed’ boundary layer from the free atmosphere. The slab model describes the BL daily evolution using three equations; the first for the temporal evolution of the mean value of potential temperature, θ , the second for the temperature increment at the inversion height, $\Delta\theta$, and the last equation for the BL height tendency, dh/dt . The principle equation of interest governs the boundary layer height since this is the variable to be retrieved (see Figure 3.6).

The time evolution of the potential temperature directly stems from the assumption of energy conservation within the mixed layer which, following [73], can be written as:

$$h \frac{d\langle\bar{\theta}\rangle}{dt} = \overline{w'\theta'}_{h_0} - \overline{w'\theta'}_h \quad (3.12)$$

where the angle brackets $\langle \rangle$ denote an average over the depth of the mixed layer and x' is the turbulent part of the variable x . $\overline{w'\theta'}_{h_0}$ and $\overline{w'\theta'}_h$ are the kinematic heat fluxes at the surface and mixed layer top, respectively, while w represents the vertical wind velocity. Since it is assumed that $\bar{\theta}$ does not vary within the mixed layer, then $\langle\bar{\theta}\rangle = \bar{\theta}$. The flux through the entrainment layer can be parametrised by means of the ‘entrainment velocity’, w_e . Given the definition

$$\Delta\bar{\theta} = [\bar{\theta}_h^+ - \bar{\theta}_h^-]$$

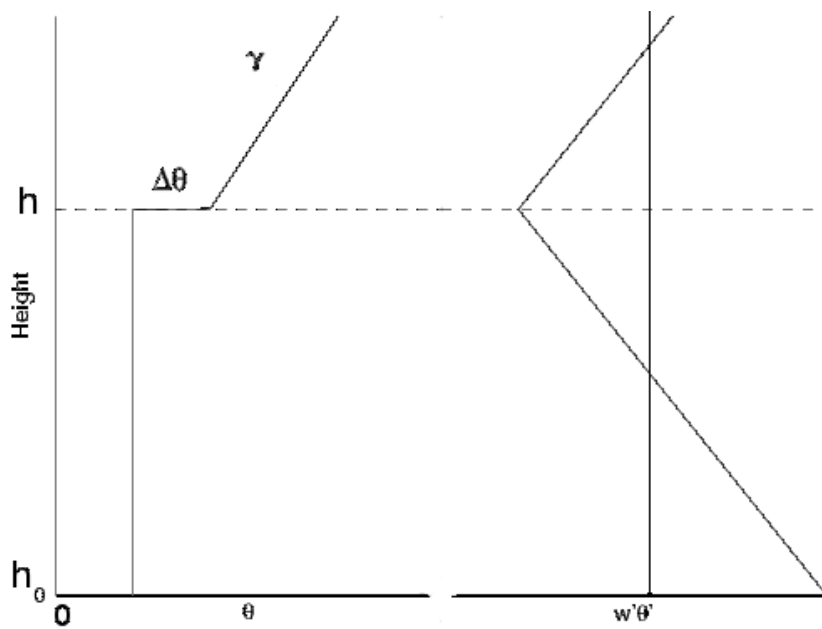


Figure 3.6: Potential temperature and kinematic turbulent heat fluxes vertical profiles for the mixed layer in the slab model. The symbols are explained in the text.

then

$$\overline{w'\theta'}_h = -w_e\Delta\bar{\theta} \quad (3.13)$$

where $\Delta\bar{\theta}$ is the temperature increment at the BL top [4].

In this simplified model, the temperature discontinuity at the BL top ($\Delta\bar{\theta}$) decreases as the mixed layer warms [75]. The process of creation and destruction of the BL is controlled by the temperature profile which is a function of the surface sensible heat flux. The equation for the time evolution of $\Delta\bar{\theta}$ therefore reads:

$$\frac{d\Delta\bar{\theta}}{dt} = \gamma w_e - \frac{d\bar{\theta}}{dt} \quad (3.14)$$

where γ is the temperature gradient above the BL. Following [24] and assuming air density constant in the mixed layer the time evolution of h is predicted by

$$\frac{dh}{dt} = w_e + w_s \quad (3.15)$$

where w_s is the mean large-scale subsidence velocity and w_e the entrainment velocity.

If γ , w_s and $\overline{w'\theta'}_{h_0}$ are supplemented as boundary conditions, then equations (3.12)-(3.15) contain five unknowns: h , $\bar{\theta}$, $\Delta\bar{\theta}$, w_e and $\overline{w'\theta'}_h$. Thus a closure assumption for one unknown must be made to solve the model \mathcal{S} .

Under the hypothesis that fluxes vary linearly within the mixing layer then we have $\overline{w'\theta'}_h = \beta\overline{w'\theta'}_{h_0}$. A value of β equal to -0.2 was suggested by [75] and is usually applied. With this suggested closure, surface heat fluxes at the surface, $\overline{w'\theta'}_{h_0}$, are needed as model boundary conditions. Fluxes are prescribed by means of a parametric function which simulate a sinusoidal daily evolution of the surface energy budget:

$$\overline{w'\theta'}_{h_0} = A_d \sin(2\pi(t_i - t)/t_d) \quad (3.16)$$

where A_d , t_i and t_d model the amplitude, phase and wavelength of surface sensible heat flux.

3.2.4 The assimilation procedure

The assimilation procedure is the novel aspect of the BSM approach and for this reason is discussed in some detail. Firstly the Bayes theorem can

be claimed to justify the use of equation (3.6) to find the optimal model solution, $\mathbf{h}_{\mathcal{S}(an)}$, i.e. the *a-posteriori* estimate of the ‘true’ BL height, given a vector of observed values, $\mathbf{h}_{\mathcal{G}}$, and *a-priori* climatology, $\mathbf{h}_{\mathcal{S}(bg)}$. Under the hypothesis of Gaussianity and no correlation between model and observation errors, it can be proved that the *a-posteriori* estimator of the state vector coincides with the minimum of the cost function given in eq. (3.6). $\mathbf{h}_{\mathcal{S}(an)}$ is thus an optimised solution of the physical-model, \mathcal{S} , described in the previous section. The optimisation is performed on the model parameter space, $\phi_1 \equiv (\gamma, w_s, \overline{w'\theta'}_{h_0})$ and not on the state vector $\mathbf{h}_{\mathcal{S}}$ itself. The set of initial values, $\phi_2 \equiv (A_d, t_i, t_d)$, needed to integrate the ordinary differential equations in (3.12), (3.14) and (3.15) are initially prescribed with fixed values, and then themselves optimised in the assimilation procedure.

The values of

$$\phi^{\mathcal{S}(an)} \equiv (\phi_1^{\mathcal{S}(an)}, \phi_2^{\mathcal{S}(an)})$$

minimising (3.6), are found by means of an efficient stochastic Monte Carlo approach, namely DRAM-MCMC [Delayed Rejection Adaptive Metropolis-Markov Chain Monte Carlo 30]. This algorithm generates a Markov chain [27] whose values are as distributed as their posterior probability distribution function (PDF). If we indicate by

$$\phi^{\mathcal{S}(l)} \equiv (\phi_1^{\mathcal{S}(l)}, \phi_2^{\mathcal{S}(l)})$$

the parameter values drawn at iteration l , using a proposal density $Q(\phi^{\mathcal{S}}|\phi^{\mathcal{S}(l)})$ which depends on the previous state, $\phi^{\mathcal{S}(l)}$ only, the algorithm accepts this proposal as the next value ($\phi^{\mathcal{S}(l+1)} = \phi^{\mathcal{S}}$) of the Markov chain if

$$\alpha < \min \left\{ \frac{p(\phi^{\mathcal{S}}|\mathbf{h}_{\mathcal{G}}, \mathbf{h}_{\mathcal{S}(bg)})}{p(\phi^{\mathcal{S}(l)}|\mathbf{h}_{\mathcal{G}}, \mathbf{h}_{\mathcal{S}(bg)})} \frac{Q(\phi^{\mathcal{S}(l)}|\phi^{\mathcal{S}})}{Q(\phi^{\mathcal{S}}|\phi^{\mathcal{S}(l)})}, 1 \right\} \quad (3.17)$$

where α is a random number uniformly drawn from the $[0, 1[$ interval, $\mathbf{h}_{\mathcal{G}}$ the vector with the experimentally estimated BL heights and $\mathbf{h}_{\mathcal{S}(bg)}$ the vector of climatological BL heights. If this condition is not verified the previous state is retained and $\phi^{\mathcal{S}(l+1)} = \phi^{\mathcal{S}(l)}$.

$p(\phi^{\mathcal{S}(l)}|\mathbf{h}_{\mathcal{G}}, \mathbf{h}_{\mathcal{S}(bg)})$ is the *a-posteriori* PDF of the vector of BL heights. If we assume this function to be Gaussian then it can be shown that the functional in (3.6) is its exponent. The minimisation of the exponent can be interpreted as the attempt of the DRAM algorithm to draw a sequence of model parameter values, $\phi^{\mathcal{S}(l)}$, as distributed as the *a-posteriori* PDF for a model to fit the given data.

3.2.5 Criteria of selection

Once the model trajectory $\mathbf{h}_{S(an)}$ is available from the assimilation procedure, it can be used to select which ceilometer-detected stratification is the best choice for h . As $\mathbf{h}_{S(an)}$ is itself a variable criterion of selection, the simplest and most obvious way to choose between stratifications is by looking at their proximity to this curve. There are nevertheless some exceptions which need to be handled. It can occur that for a given time, no stratification is detected by the ceilometer or that the ceilometer initial retrieval h_G is very far from the expected climatological values $h_{S(bg)}$. In both these cases the decision is made to adopt $\mathbf{h}_{S(an)}$ at that time as the best estimation of the boundary layer height. It has to be noted then that even in these cases, while $\mathbf{h}_{S(an)}$ is not a marked point from the ceilometer data processing, it still retains information on the actual ceilometer scene. In fact $\mathbf{h}_{S(an)}$ is itself obtained by the assimilation process which selects the “optimal” (in statistical sense) model trajectory for the day given the set of ceilometer observations.

To be consistent with the rule of excluding the selection of heights too distant from the climatology a preliminary quality control is also applied to reject points where $|h_G - h_{S(bg)}| > d_{\max}$, where d_{\max} is two times the estimated standard deviation (i.e. the diagonal elements of \mathbf{E}).

3.3 BSM implementation

The method outlined in the previous section is now analysed in the light of a practical application. It will be shown that in the BSM actual implementation a series of empirical choices (tuning parameters) have to be made whose impact on the final boundary layer height estimations need to be verified and tested, possibly by means of independent observations. For this reason sensitivity studies and a verification section are provided. They attempt to assess the retrieval performance of the BSM technique when applying the methodology to a long time series of observations collected by a lidar-ceilometer.

The period chosen for verification coincides with the four months observational phase of the Budget of the Atmosphere-Soil Exchange: A Long-term Fluxes Analysis (BASE:ALFA) project. The BASE:ALFA dataset has been collected at San Pietro Capofiume (SPC) in the middle of the Po Valley where a operating observing station managed by ARPA-SIMC is in place since 1984. The whole experimental period covers two IOPs; one during

the summer season between the 18th of June 2009 and the 18th of July 2009 and one in winter-spring, between the 18th of January and the 18th of April. During these two phases an intensification of radiosonde launches was planned when the development of convective or stratified BL conditions. Up to 4 radiosoundings per day at synoptic times (00,06,12,18 UTC) guarantees the independent characterisation of the full evolution of the vertical BL processes.

In addition to the conventional meteorological measurements including surface and upper air observations for the BASE:ALFA project, SPC was equipped with a commercial lidar-Ceilometer, Vaisala LD-40 from ISAC-Rome, which provided the remote observation of the boundary layer evolution under very diverse meteorological conditions. The raw ceilometer signal has been processed as explained in section 3.2.2. The retrieval of BL heights from the radiosoundings profiles are obtained by subjectively inspecting the virtual potential temperature profile. The [33] method is applied for unstable conditions⁶. It follows the idea that an air parcel leaving the ground with a given surface potential temperature can reach the height where the atmosphere has the same potential temperature, which is then taken as the BL height. On the contrary, in a stable BL the empirical inspection of the potential temperature profile leads to evaluate the height at which there is the transition from stable to neutral conditions, possibly matching with inflection points of dry temperature, specific humidity and wind speed. It has to be noted that radiosoundings are not currently used as a reference under the difficult stable conditions, thus the nocturnal cases should be compared to this reference with caution. Moreover the method used to determine the PBL height by radiosonde is a subjective analysis of vertical profiles achieved by repeating the analysis by three independent people and calculating the standard deviation of the three values, which was smaller than 5%. This is then given as an estimate of the h_{RDS} precision. The accuracy on h_{RDS} is instead not evaluable being h_{true} an unknown. A total of 174 radiosounding profiles have been processed and form the statistical basis for the successive verification of the BSM method.

⁶The distinction between stable and unstable conditions is made on the basis of the sign of the sensible heat flux at the surface, H_s . If $H_s > 0$ the BL is considered unstable, if $H_s < 0$ stable

3.3.1 Initial h estimates: $\mathbf{h}_{\mathcal{G}}$

The BSM assimilates initial h estimates to find an optimised $\mathbf{h}_{\mathcal{S}(an)}$ model solution. These values, which are elements of the vector $\mathbf{h}_{\mathcal{G}}$ in equation 3.6, should be provided by a preliminary automated evaluation of the ceilometer scene. Operator-based (that is manual) choice of BL heights from the ensemble of marked stratifications are likely to be more accurate than any automated choice, nevertheless in this context the aim is to provide a final retrieval of h without the aid of an operator. Therefore three different selection criteria are tested as initialisation of $\mathbf{h}_{\mathcal{G}}$. In the first the vertical height corresponding to the highest value of the first $S \times R^2$ derivative or the highest value of the convolution function between the $S \times R^2$ and the wavelet is taken as retrieved BL height (experiment G1). The second 1D retrieval choice selects inflection points possessing the smaller standard deviation (experiment named G2) which is equivalent to the selection of the sharpest stratification. Finally, the third strategy adopted simply selects the lowest inflection point, i.e. the first vertical stratification identified by the ceilometer above the blind zone of 60 m (experiment named G3). $\mathbf{h}_{\mathcal{G}1}$, $\mathbf{h}_{\mathcal{G}2}$, $\mathbf{h}_{\mathcal{G}3}$, when the ceilometer signal is processed using the gradient method or $\mathbf{h}_{\mathcal{G}1w}$, $\mathbf{h}_{\mathcal{G}2w}$, $\mathbf{h}_{\mathcal{G}3w}$, when the ceilometer signal is processed using the wavelet approach, are, in the following, both used to initialise the assimilation procedure of the BSM method and to assess its performance. Table 3.2 summarises the 6 experiments.

The sensitivity of the final $\mathbf{h}_{\mathcal{S}(an)}$ to any initial $\mathbf{h}_{\mathcal{G}}$ is reported in figure 3.7 for the day of example showed in figure 3.1 and for the G1_w, G2_w, G3_w experiments. The initial climatological solution of the bulk model, $\mathbf{h}_{\mathcal{S}(bg)}$, which is also the starting point of any of the three iterative procedures is also reported for reference (solid black line). The $\mathbf{h}_{\mathcal{S}(an)}$ prediction is heavily driven by $\mathbf{h}_{\mathcal{G}}$. In our example case a strong residual layer is present between 00am and 10am. Higher stratification edges are erroneously selected by both the G1_w and G2_w experiments. The assimilation of these points into the BSM modifies the initial background estimation, $\mathbf{h}_{\mathcal{S}(bg)}$, and produces a prediction for a too fast growing boundary layer in the morning and a too slow decline in the evening. For this specific day, therefore, h_{BSM} obtained from the G3_w assimilation provides the closest agreement with the subjective analysis of the ceilometer scene as performed by an experienced analyser (also reported on the plot with black crosses for completeness). Nevertheless, the long term statistical verification which follows in the next section will prove that on average G1_w, G2_w and G3_w provide a similar performance.

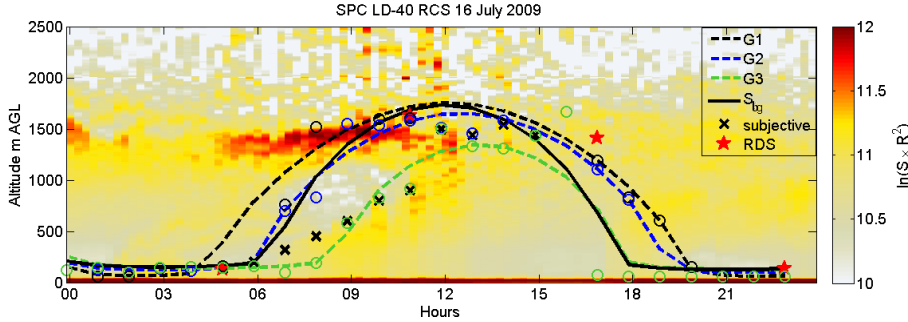


Figure 3.7: $h_{S(an)}$ predictions as a function of h_G for the three $G1_w$, $G2_w$, $G3_w$ experiments. The initial background estimation $h_{S(bg)}$ (black line) is reported for completeness. The scene has been subjectively evaluated and the most probable BL height marked by an experienced analyst. Available h from radiosoundings are reported with red stars.

3.3.2 Error estimation: \mathbf{E} and \mathbf{B} matrices

A critical point in the minimisation of the cost function in equation (3.6) is the estimation of the model and the observation uncertainties which are needed to calculate the two dimensional error covariance matrices \mathbf{B} and \mathbf{E} in equation (3.6). In practical terms, \mathbf{B} and \mathbf{E} provide the tolerance to the fit search and therefore drive the convergence of the minimisation process defined by equation 3.6.

The diagonal elements of the \mathbf{B} matrix are the estimated root-mean-square-errors (RMSE) of the model background (climatology) at each instant during the day. The off-diagonal elements of \mathbf{B} represent climatological cross-correlation errors at different times during the day. For simplicity in this study the \mathbf{B} matrix is assumed diagonal, i.e we neglect cross-correlation errors. Ideally \mathbf{B} should be constructed using the climatology of model minus observed departures. Since only a few benchmark estimates of h from radiosoundings are available at limited synoptic hours the conservative assumption is made that model errors on h could be well represented by their climatological spread. In fact the amplitude of the \mathbf{B} elements is likely to be strongly influenced by weather regimes and seasonality. The climatological variability in mixing heights predicted by the slab model was then estimated using a vast set of atmospheric profiles provided by the simulations of a

limited-area model. Outputs of the COSMO⁷ model are produced daily at ARPA-SIMC by the operational weather forecasting system and they are available at SanPietroCapofiume location for the whole BASE:ALFA period at hourly resolution. Therefore, the bulk model, \mathcal{S} , has been initialised each day by the COSMO fields and mixing height predictions stored to create a climatological monthly dataset. The mean value from the dataset is then used as initial background estimation ($h_{\mathcal{S}(bg)}$) while its RMSE is used for the diagonal elements of the \mathbf{B} matrix.

Figure 3.8 shows the diagonal elements of \mathbf{B} as estimated for the four months corresponding to the verification period. A higher BL height variability is predicted during daytime and in the summer period. This is due to the deeper vertical development of the BL in warm conditions. A smaller variability (in terms of RMSE) is clearly predicted in stable atmospheric conditions mostly occurring during night.

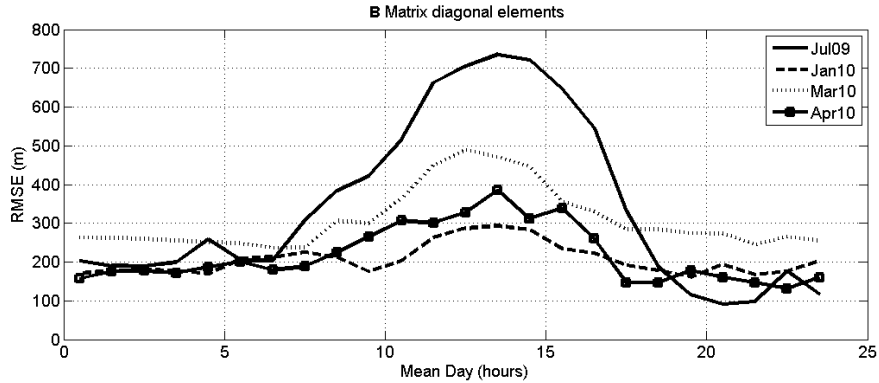


Figure 3.8: Root mean square errors for the slab model \mathcal{S} . These estimations are used to fill the diagonal elements of the \mathbf{B} matrix for the four months corresponding to the verification period.

The way error estimates can be obtained for the h_G vector has been explained in section 3.2.2. Since h_G values are calculated on each single 1D column the assumption to neglect the cross-diagonal elements of \mathbf{E} seems quite reasonable in this case. Clearly each of the six experiments (G1, G2, G3, G1_w, G2_w, G3_w) will have a different \mathbf{E} . Figure 3.9 shows the daily average for the four months of the verification period. By definition G2, G2_w

⁷The regional model COSMO is developed in within the COSMO consortium full details can be found on www.cosmo-model.org

possesses the smallest RMSE. The larger dispersion of the G1,G1_w ensemble is possibly due to the sharper gradients introduced by greater noise-induced signal variability at the upper levels with respect to lower ones. In fact, the variability is larger in summer, when the top layers are further away from the ceilometer and in sunlit periods, when the background noise is maximum.

3.3.3 Model background: \mathcal{S}_{bg}

In optimal estimation theory the starting point of the iterative procedure which leads to the minimisation of the cost function J in equation 3.6 should be unimportant. For linear systems the minimum of J is found at the first iteration, whatever the initial vector $\mathbf{h}_{\mathcal{S}}$ is. Due to non-linearities in \mathcal{S} however a first guess $\mathbf{h}_{\mathcal{S}}$ that is very distant from the real state could result in the minimisation being trapped, for example, in a local function minimum. The choice made in this study is to initialise the iteration procedure from the climatological prediction, i.e. to use the same $\mathbf{h}_{\mathcal{S}(bg)}$ vector.

$\mathbf{h}_{\mathcal{S}(bg)}$ is the monthly climatological value of \mathcal{S} . Another choice could be, for example, to use the daily available analysis from the COSMO model. There were some practical considerations in support of the use of climatological values. Firstly, the simplicity of the bulk model should minimize problems related to the convergence procedure. Moreover errors on $\mathbf{h}_{\mathcal{S}(bg)}$ are conservatively set to the same magnitude as the climatological $\mathbf{h}_{\mathcal{S}}$ itself therefore allowing very large increments during the minimisation procedure. Finally, the emphasis here is to propose a method that can be applied in the context in which forecast model runs are not in general available.

Sensitivity tests (not shown) performed using the COSMO daily prediction of $\mathbf{h}_{\mathcal{S}(bg)}$ instead of the monthly climatological value shows no significant differences. The large estimated error in the climatology results in the final analysis predominantly controlled by the ceilometer measurements (i.e. $\mathbf{h}_{\mathcal{G}}$).

3.4 Method assessment

The BSM method is a selection technique which conveys in time information detected locally by a ceilometer data processing algorithm. The accuracy of the BSM in determining h , therefore relies heavily on the capability of the lidar to mark the PBL mixing height. In the extreme case in which, for example, the data analysis applied to the ceilometer scene either using the wavelet

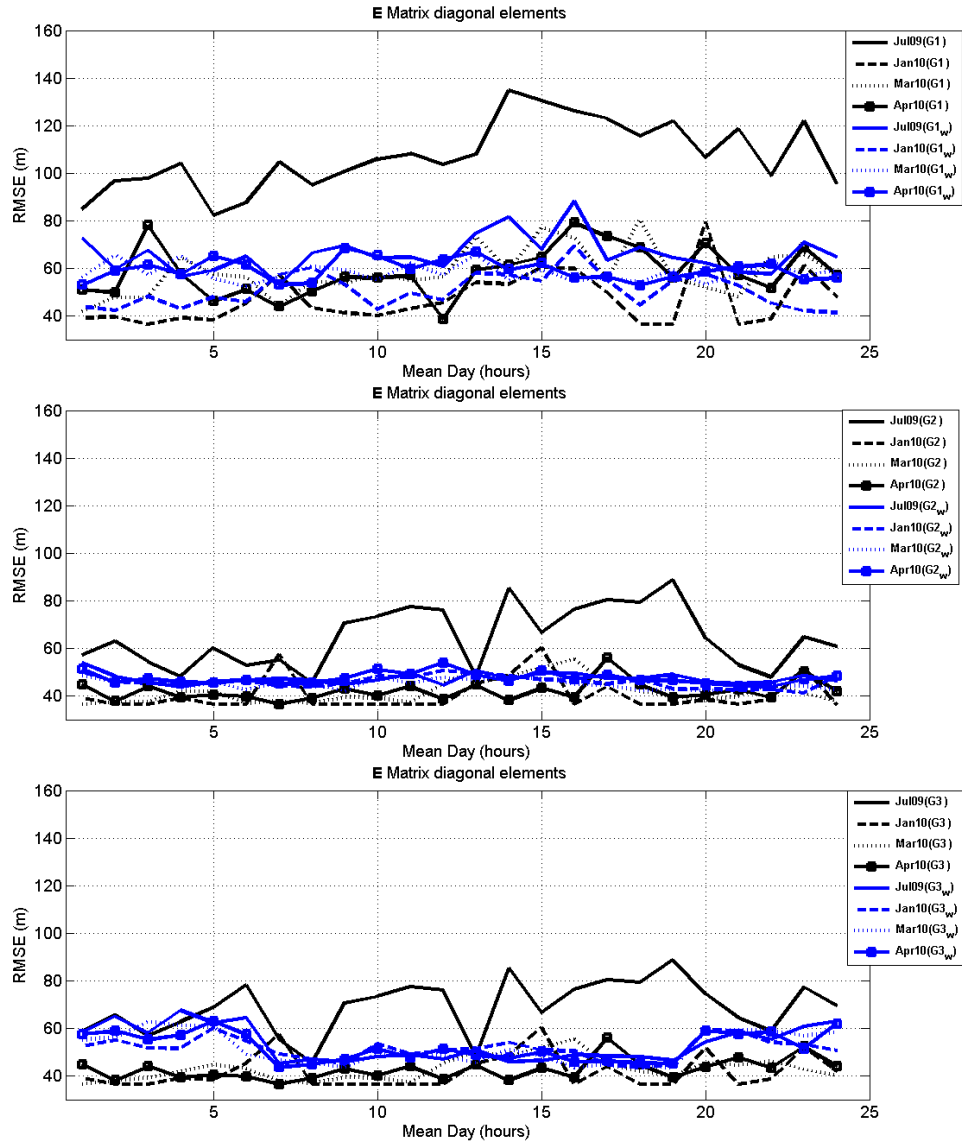


Figure 3.9: Diagonal elements of the observational error covariance matrix \mathbf{E} . The estimations refer to the four months corresponding to the verification period and for the six different 1D retrievals (G1, G2, G3) when the gradient method is applied to the ceilometer data and (G1_w, G2_w, G3_w) when the wavelet method is applied. See text for further details.

or the gradient approach only provided rejected data points (for example a foggy day) then the BSM would furnish a climatological estimation of the h evolution. We expect the BSM method to work at its best when disturbances in the backscatter signal cause the other approaches to fail to select between all the stratifications marked the most probable PBL height. To show how the BSM uses in an “optimal” statistical way information already deduced from the ceilometer scene data analysis, a set of comparisons is performed against the 1D selection criteria typified by experiments marked G1, G2 and G3 both applying the gradient or wavelet approach. The main aim of this comparison is to prove the usefulness of the BSM approach for an automated detection of h from low cost lidar-ceilometer instruments.

3.4.1 Direct validation: comparison to radiosoundings

Comparisons between the BSM and standard automated detection algorithms and radiosounding BL height estimations are shown in figure 3.10 for the whole four month period. The correlation, expressed in terms of the correlation coefficient and the root-mean square error between the ceilometer and radiosounding estimates is in general poor, independently of the criterion of selection applied to the $S \times R^2$ data processing. This result highlights the difficulty for a 1D retrieval method based on fixed thresholds on the $S \times R^2$ to robustly mark the right stratification edge as boundary layer height. A more flexible criterion is clearly needed. It has to be stressed that the BASE:ALFA dataset spans contrasting meteorological conditions. Nevertheless, the main aim here is to test a retrieval method which is robust enough to be used for the operational monitoring of the BL evolution. Therefore the statistical performance of the BSM using a long term dataset is considered crucial in this context.

The same analysis is reported in Figure 3.11 but for the BSM approach applied to the same ceilometer dataset and with one of the (G1, G2, G3) or ($G1_w$, $G2_w$, $G3_w$) experiments used as observation to find the slab model trajectory (\mathbf{h}_G in equation 3.6). Starting from any of the G experiments does not greatly modify the quality of the retrieved height. Therefore in the following for ease of representation only the G1 and $G1_w$ experiments will be shown. This result highlights that the BSM provides robust predictions almost independently of the initial choice of \mathbf{h}_G . Using the BSM approach the correlation between ceilometer and radiosounding estimations is greatly improved and the mean root-mean-square error substantially reduced.

On average the BSM is able to perform well in all sky conditions. Nevertheless, most of the benefit arises from a better performance during nighttime ($h < 500$ m). The (1D) wavelet (or gradient analysis) detects strong stratifications due to nocturnal residual layers which are high and do not match the radiosonde estimates.

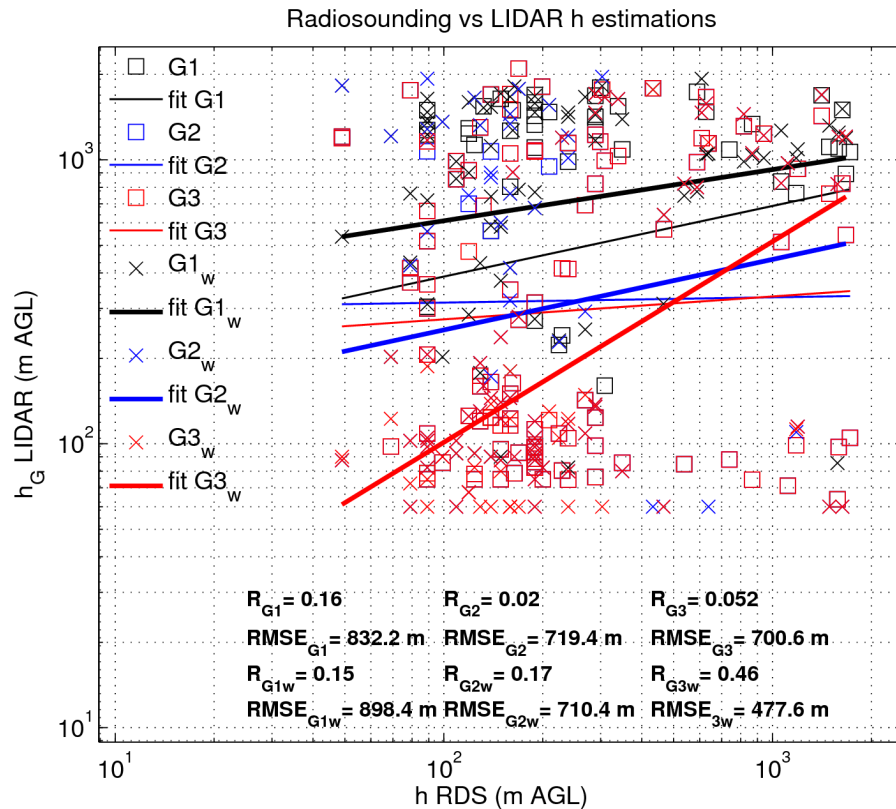


Figure 3.10: Ceilometer versus radiosounding BL heights for the whole four month period of the BASE:ALFA dataset. Different ceilometer retrieval approaches are taken as h_G . Specifically the ceilometer signal strongest discontinuity, the sharper atmospheric layer detected and the lowest signal discontinuity border. The analysis is repeated using the gradient (experiments G1, G2, G3) and the wavelet data analysis (experiments $G1_w$, $G2_w$, $G3_w$)

This distinction between the approaches is highlighted in figure 3.12 which shows a week during July 2009 in which 4 radiosounding a day were available.

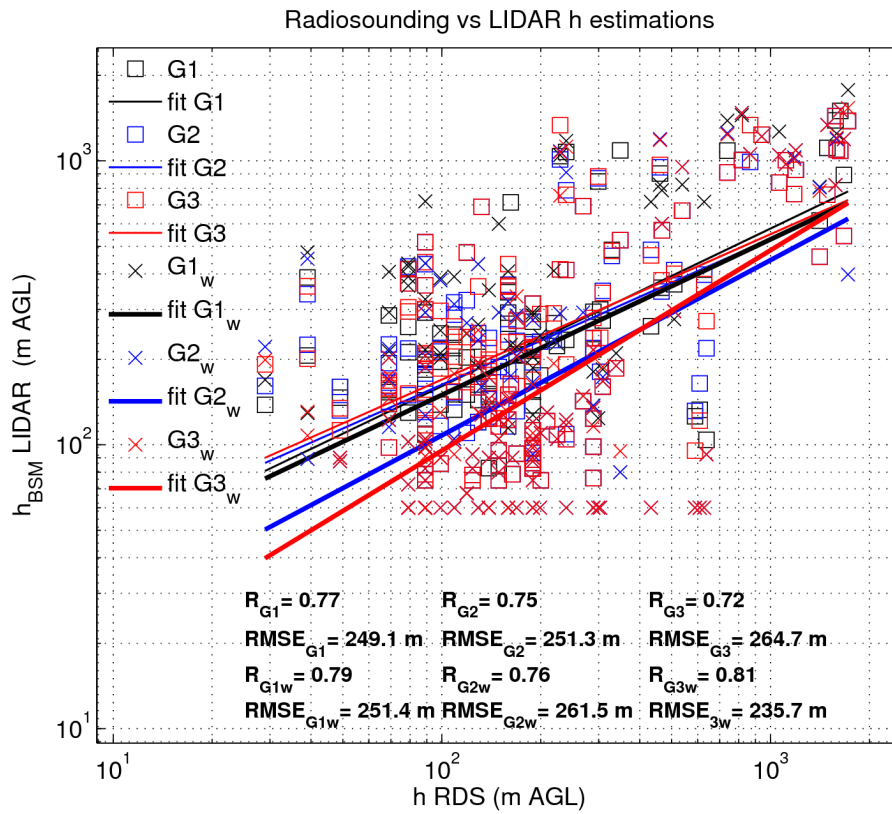


Figure 3.11: As Figure 3.10 but for the BSM approach.

Only gradient and wavelet retrievals from $G1$ and $G1_w$ are shown. It is evident how a column-by-column 1D processing of the ceilometer signal which misses a-priori information on the expected physical evolution of the BL fails to correctly identify h among all signal discontinuities. The discrepancies are larger at nighttime when residual layers can generate very strong ceilometer signals which are classified by the gradient/wavelet methods as the most probable BL height. The BSM approach instead carries information on the low climatological probability to find very deep BLs during nighttime and therefore penalises the selection of high stratifications with respect to lower ones.

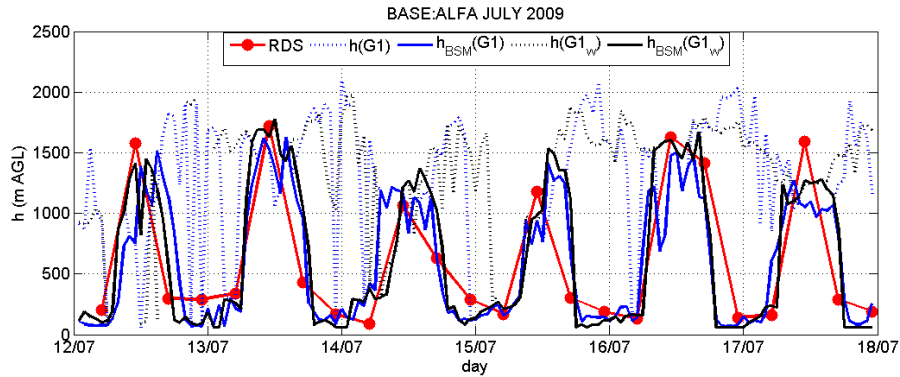


Figure 3.12: Daily course of h estimations for a week during July 2009 in which 4 radiosounding a day were available. The BSM method is compared to 1D selection methods and benchmark estimations from radiosounding profiles.

The analysis of the BSM algorithm in some specific synoptic regimes helps to evaluate its all weather capability when compared to the $G1$ approach (the $G2$ and $G3$ experiments gave similar results and are omitted). In Figure 3.13 some selected days from the BASE:ALFA verification period are analysed in detail. The a) and c) panels show the evolution of the boundary layer in clear sky conditions. The presence of fog in the early morning from 05 UTC to 08 UTC is visible in panel c). Fog saturates the ceilometer $S \times R^2$ and prevents the detection of any stratifications in those hours, as a consequence some h_G are not available. The BSM instead is able to provide a continuous estimation and to fill these gaps. One of the most relevant properties of the BSM method is therefore to be able to correctly convey information during time, which otherwise, would not be available from the column-by-column analysis of the raw ceilometer signal. In the following hours the BL develops

and the two methods give identical results. In the late afternoon, the G1, G1_w methods start to select a strong stratification due to the residual layer. The BSM method instead correctly chooses stratifications near the surface produced by the stable BL.

In figure 3.13 panels b) and d) two cloudy cases are shown. In convective and stratiform conditions ceilometer processing is considered ineffective. In panel d) the stratus cloud is located well above the BL. Nevertheless the G1 algorithm in the central part of the day is unable to detect stratifications. Again the BSM provides a continuous estimations of h by transferring the information from the few observations available. In the case depicted in panel b) a convective updraught is developing during the day which generates an early afternoon shower. The ceilometer signal saturates in presence of clouds. Moreover aerosol suspensions are washed out by the precipitation event. The classical 1D methods provide in this case a problematic BL retrieval with a very unpredictable selection of stratifications as progressing during the day. The BSM estimation is likely to be erroneous as well. The estimated mid-day h is suspiciously located where the maximum of turbulence occurs (entrainment processes at the cloud top). It is nevertheless evident that from 17UCT onward the BSM approach is able to select the most probable BL height among the whole set of stratifications identified.

It should be stressed that the use of $\mathbf{h}_{S(an)}$ in place of a detected ceilometer point is *not* equivalent to the use of a model climatological prediction. In fact $\mathbf{h}_{S(an)}$ is generated by assimilating available observations at all times. Therefore, $\mathbf{h}_{S(an)}$ is itself the mechanism with which the BSM conveys observation information in time for a specific scene. To show how this assimilation procedure already contains all the relevant information and is therefore appropriate to be used in place of detected ceilometer stratifications, figure 3.14 shows how the correlation of $\mathbf{h}_{S(an)}$ for the G1_w, G2_w and G3_w cases with respect to the benchmark RDS estimates is almost equivalent the result obtained using $\mathbf{h}_{S(an)}$ to re-select the ceilometer points. $\mathbf{h}_{S(an)}$ is obtained assimilating the 24 daily predictions of h to calculate 6 parameters of the bulk model

$$((\phi_1^{\mathcal{S}(an)}, \phi_2^{\mathcal{S}(an)})$$

and fewer points could be sufficient to determine the curve. The immediate benefit is that a longer average data window could be applied to improve the signal-to-noise ratio of the lidar-ceilometer employed. The model climatology, $\mathbf{h}_{S(bg)}$ also shows a good correlation with the RDS data. Since most of the

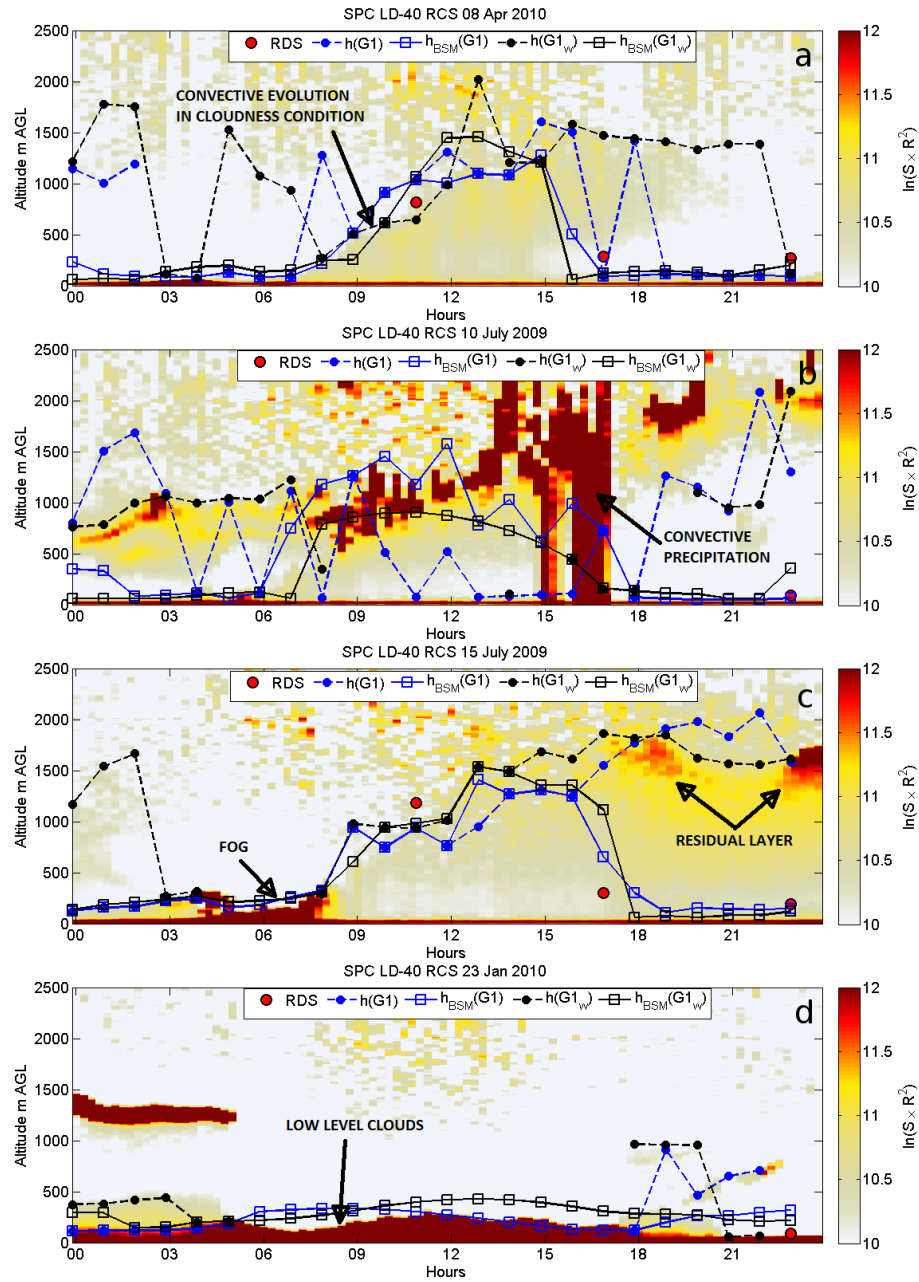


Figure 3.13: Ceilometer back-scatter signal and boundary layer height estimation on April 8th, 2010 (panel a); July 10th, 2009 (panel b); July 15th, 2009 (panel c); and January 23th, 2010 (panel d). squares are h estimates from the G1 experiments, dots are used for the BSM estimated BL heights. Isolated dots are benchmarks RDS estimations.

error in our dataset comes from the wrong prediction of h at nighttime at these times even the climatological value of h is able to improve on the simple 1D estimates. While this analysis is useful to assess the role played in turn by the climatology and the assimilation procedure in the BSM, it should be nevertheless emphasized that by having radiosounding each 3 hours (and not mostly at 00UTC) would allow a better sampling of the BL daily evolution with a consequent more robust assessment of the differences between $h_{S(an)}$ and $h_{S(bg)}$.

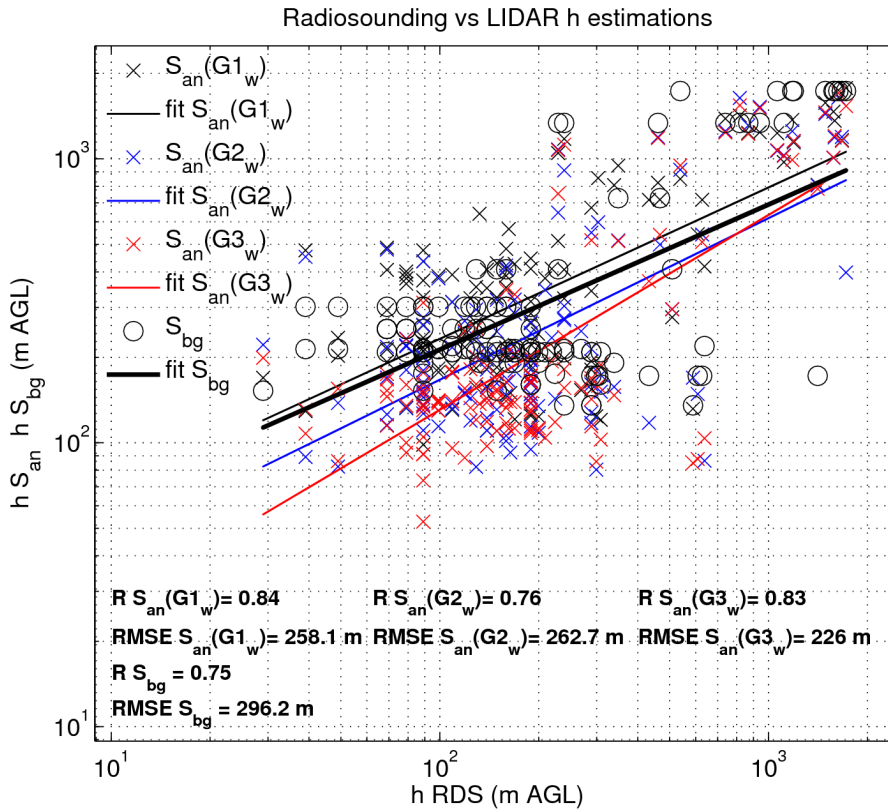


Figure 3.14: $h_{S(an)}$ and $h_{S(bg)}$ versus radiosounding BL heights for the whole four month period of the BASE:ALFA dataset.

3.4.2 Indirect validation: comparison to black carbon concentration

One of the main reasons to design and develop the BSM method was the need for the continuous monitoring of ceilometer derived BL heights. For example, a reliable estimation of retrieved boundary layer height is crucial in any application related to air quality forecasts. From the point of view of chemical transport models, the BL height is an input parameter characterising the vertical dilution capability of the BL. As a zero order approximation, the deeper the BL the more diluted the pollutants become. Thus higher concentrations are expected at nights when BL is very low in stable conditions.

A measurement campaign of the AEROCLOUDS (Study of the Direct and Indirect Effects of Aerosols and Clouds on Climate) project was also conducted during the summer IOP of the BASE:ALFA project in the same location of San Pietro Capofiume. In the framework of the AEROCLOUDS project, black carbon (BC, a fraction of anthropogenic aerosol) was measured by using a Particle Soot Absorption Photometer (PSAP). The PSAP measures the particle absorption coefficient b_{abs} at 573 nm. The concentration of black carbon [BC] is then calculated assuming a specific absorption cross section $\sigma_{abs} = 13m^2/g$ [S.De Cesari and C.Lanconelli, personal communication]. BC has been selected as a good tracer of primary anthropogenic pollution. It can only be produced in a combustion process and is therefore solely primary [69]. It has a typical lifetime between 6 and 10 days, being involved only in chemical processes which occur in the mixing layer [11].

Figure 3.15 shows for two weeks in summer 2009 the concentration of the black carbon [BC] as compared to the boundary layer depth as estimated by the BSM approach and the normal gradient method (experiments G1 and G1_w). h_{BSM} better explains the typical daily course of [BC], with lower concentrations often occurring during the daytime and higher concentrations during the night. On the contrary, the oscillations of h_{G1} and h_{G1_w} during the night do not correspond with oscillations in [BC].

Also some episodes of “fumigation”, which is a process where a growing mixing layer mixes elevated smoke plumes down to the ground, are recognisable and find a fine correspondence with the growth of h_{BSM} during the morning. The sudden peaks of [BC] occurring during the morning of day 16 July are probably due to the mixing of cleaner air below with a more polluted residual layer above. Ceilometer reflectivity data in figure 3.16 confirm this hypothesis. They show the $S \times R^2$ detected from the surface up to 2500m

above ground level. In the late afternoon of day 15 July, aerosol is advected to about 1000-1500 m in height, and persists in the residual layer all night long. During the morning of day 16 July the mixed layer grows from the surface up to the height of the residual layer; when the polluted layer is reached, its aerosol content (including BC) is diffused throughout the whole mixing layer, leading to a sudden increase of [BC] at the surface.

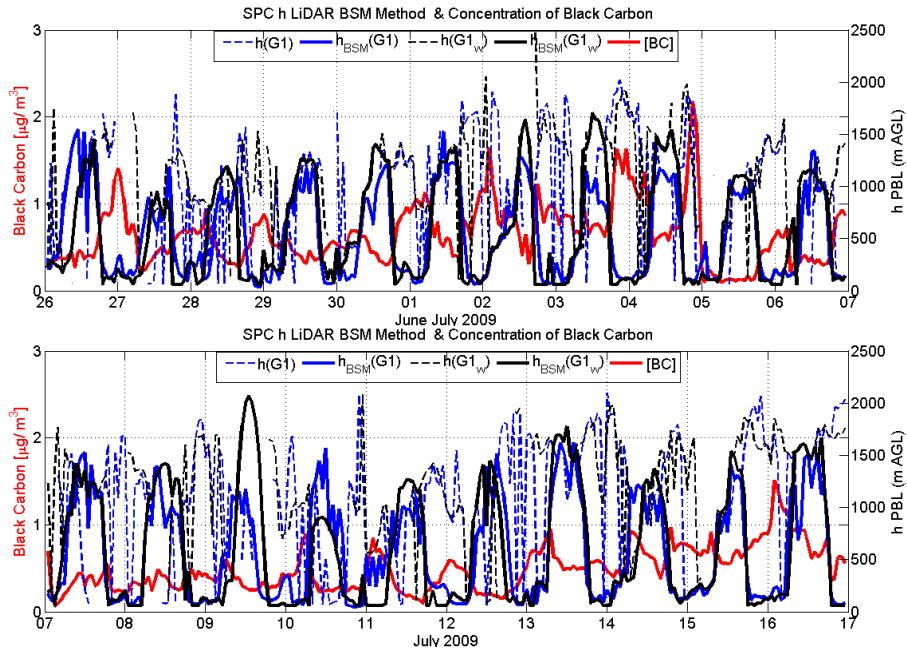


Figure 3.15: Daily course of Black Carbon concentration, [BC], from 26 of June to 17 of July 2009 as compared to the boundary layer depth as estimated by the BSM approach and the gradient or wavelet methods (experiment G1 and G1_w)

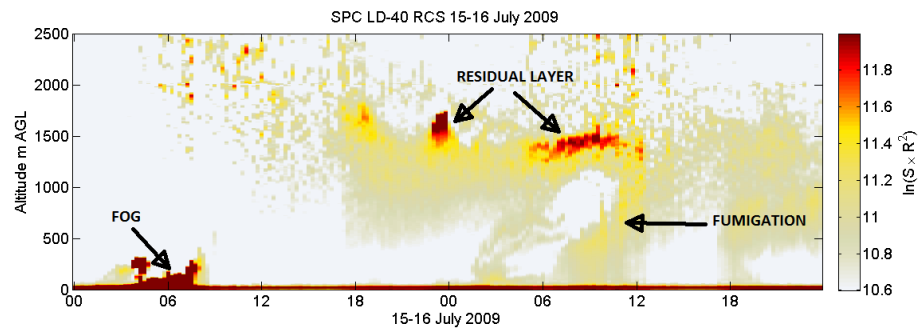


Figure 3.16: Ceilometer range corrected signal from 15 to 16 of July 2009. In the early morning of day 15 July a fog episode is recognisable; then, during the night a residual layer is detected; in the late morning of day 16 July a “fumigation” episode occurred.

Table 3.1: Summary of methods applied to boundary layer height (BLH) calculations.

	Method	Criterion	Comment
Model	Gradient number (R_g)	Richardson $R_g(z = BLH) > R_g^{crit}$ where: $R_g(z) = \frac{g}{\theta_v(z_0)} \frac{\partial \theta_v}{\partial z} \setminus \left[\left(\frac{\partial u}{\partial z} \right)^2 + \left(\frac{\partial v}{\partial z} \right)^2 \right]$ and $R_g^{crit} = 0.5$	This method is implemented in the pre-processing of the chemical transport model CHIMERE which will be used as air quality system
	Bulk Richardson number (R_b)	$R_b(z = BLH) > R_b^{crit}$ where: $R_b(z) = \frac{gz}{\theta_v(z_0)} \frac{\theta_v(z) - \theta_v(z_0)}{u(z)^2 + v(z)^2}$ $z = z_1, \dots, z_n$ are the model layers and $R_b^{crit} = \begin{cases} 0.22 & \text{in unstable conditions} \\ 0.33 & \text{in stable conditions} \end{cases}$	stability condition $H_s = \begin{cases} \geq 0 & \text{in unstable conditions} \\ < 0 & \text{in stable conditions} \end{cases}$
	Total Kinetic Energy (TKE)	$TKE < TKE_{max} r$ where: $r = \begin{cases} 0.3 & \text{unstable conditions} \\ 0.1 & \text{stable conditions} \end{cases}$	Stability condition: $H_s = \begin{cases} \geq 0 & \text{unstable conditions} \\ < 0 & \text{stable conditions} \end{cases}$
Obs	Radiosounding profiles	Holzworth [33] in unstable conditions empirical in stable conditions	Stability condition: $H_s = \begin{cases} \geq 0 & \text{unstable conditions} \\ < 0 & \text{stable conditions} \end{cases}$
	LiDAR	Wavelet Covariance Transform (WCT) method+ Bayesian regularization following [18]	

Table 3.2: Summary of the six experiments set by the choice of h_G .

Exp Name	Signal Processing	Description
G1 _w	Wavelet	Stratification corresponding to the highest value of the first $S \times R^2$ derivative
G2 _w	Wavelet	Sharpest stratification corresponding to the one with the smaller vertical spatial variance
G3 _w	Wavelet	Lowest stratification (above the blind zone of 60 m)
G1	Gradient	Stratification corresponding to the highest value of the first $S \times R^2$ derivative
G2	Gradient	Sharpest stratification corresponding to the one with the smaller vertical spatial variance
G3	Gradient	Lowest stratification (above the blind zone of 60 m)

Chapter 4

Applications

4.1 Models and Measurements Comparison

From the 4 month dataset, a summer and a winter week have been extracted to be analysed in some details. During the summer week, between the 12th and the 18th of July, Italy was mainly under a very stable high pressure system which weakened the 17th due to the arrival of a bubble of cold air from the arctic regions. Similar synoptic conditions were recorded during the winter case, between the 6th to the 10th of April 2010, when a high pressure ridge formed over the Balkans, which brought intrusion of warm and dry Saharan air. The whole Mediterranean basin was, then, characterised by good weather and poor precipitation. In these synoptic scenarios the weather conditions are driven by the surface forcing and all relevant thermodynamical processes take place in the BL. Both these periods were characterised by a weak large scale forcing which allowed the daytime growth of the BLH.

For the periods selected a chain of model simulations have been performed and output fields have been compared to the collected observation. Regional meteorological forecasts are done with the R-NWP model COSMO, forced by the ECMWF IFS model, which provides hourly initial and boundary conditions. In cascade the chemical transport model CHIMERE is run as air quality system. COSMO is a non-hydrostatic grid-point model and includes an explicit-Eulerian horizontal advection scheme and a full set of physical parametrizations for large scale condensation [72], convection [76], radiation [63] and surface processes. In these simulations we use the operational implementation of ARPA-SIMC (COSMO-I7) where the horizontal model domain

is set to cover Italy, the major part of the Mediterranean sea and the Alpine region (see fig.4.1 for the operational domain specification). The grid size is 7 km and there are 40 levels in the vertical between the surface and the top of the troposphere at around 30 hPa.



Figure 4.1: Operational domain specification for the limited area model COSMO-I7 used as numerical weather forecasting system and the chemical transport model NINFA used as air-quality forecasting system in the framework of the modelling activities of BASE:ALFA

An example of COSMO-I7 derived humidity and temperature fields compared against the radiosonde is provided in figures 4.2 and 4.3 for the two weeks selected. The general trend of the forecast agrees well with the observations even if some differences are noticeable. Lines of constant potential temperature are natural flow pathways, in an adiabatic motion, and the BL growth during the day is clearly visible. It is sustained by the longwave and shortwave downwelling forcing which is relevant in absence of cloudiness. The COSMO prediction tends to have a stronger diurnal cycle and, a preliminary evaluation of the daytime boundary layer height using the [33] method applied to both model and radiosoundings (white triangles), highlights that COSMO tends to underestimate this quantity. In general the predicted BL will result too mixed even if too shallow. There are two possible schemes which can produce these deficiencies. Either there is an overestimation of the surface turbulent fluxes due to the soil-vegetation-atmosphere transfer scheme or there is a wrong tuning of the coefficients for the momentum transfer in the turbulent scheme. In the first case the SVAT module should be investigated, in the second case the turbulence scheme.

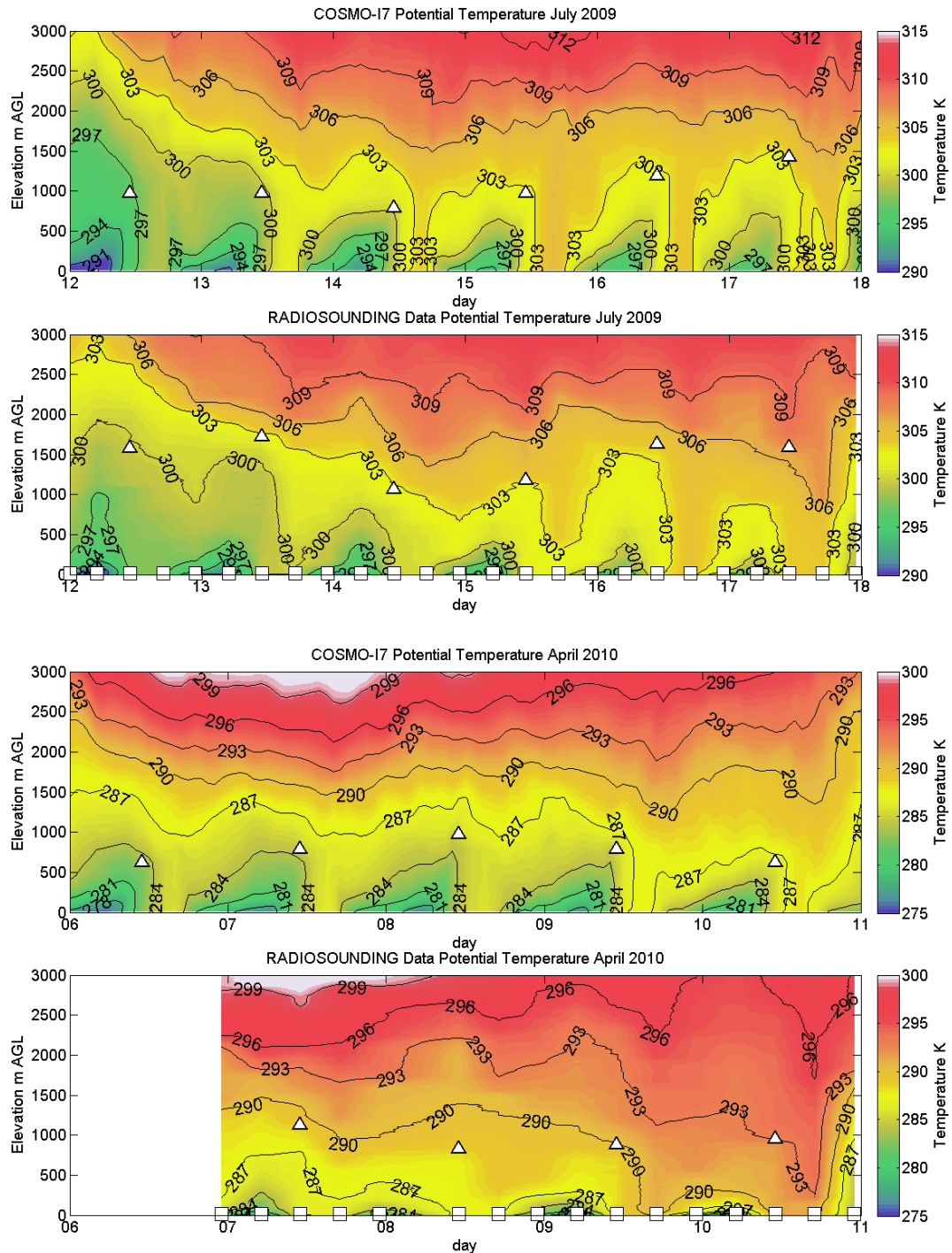


Figure 4.2: COSMO-I7 derived potential temperature fields compared against the radiosonde measurements which were collected with a maximum resolution time of 6 hours. The white square represent the instants of the radiosound launching. An evaluation of the daytime boundary layer height using the [33] method applied to both model and radiosoundings is reported with the white triangles

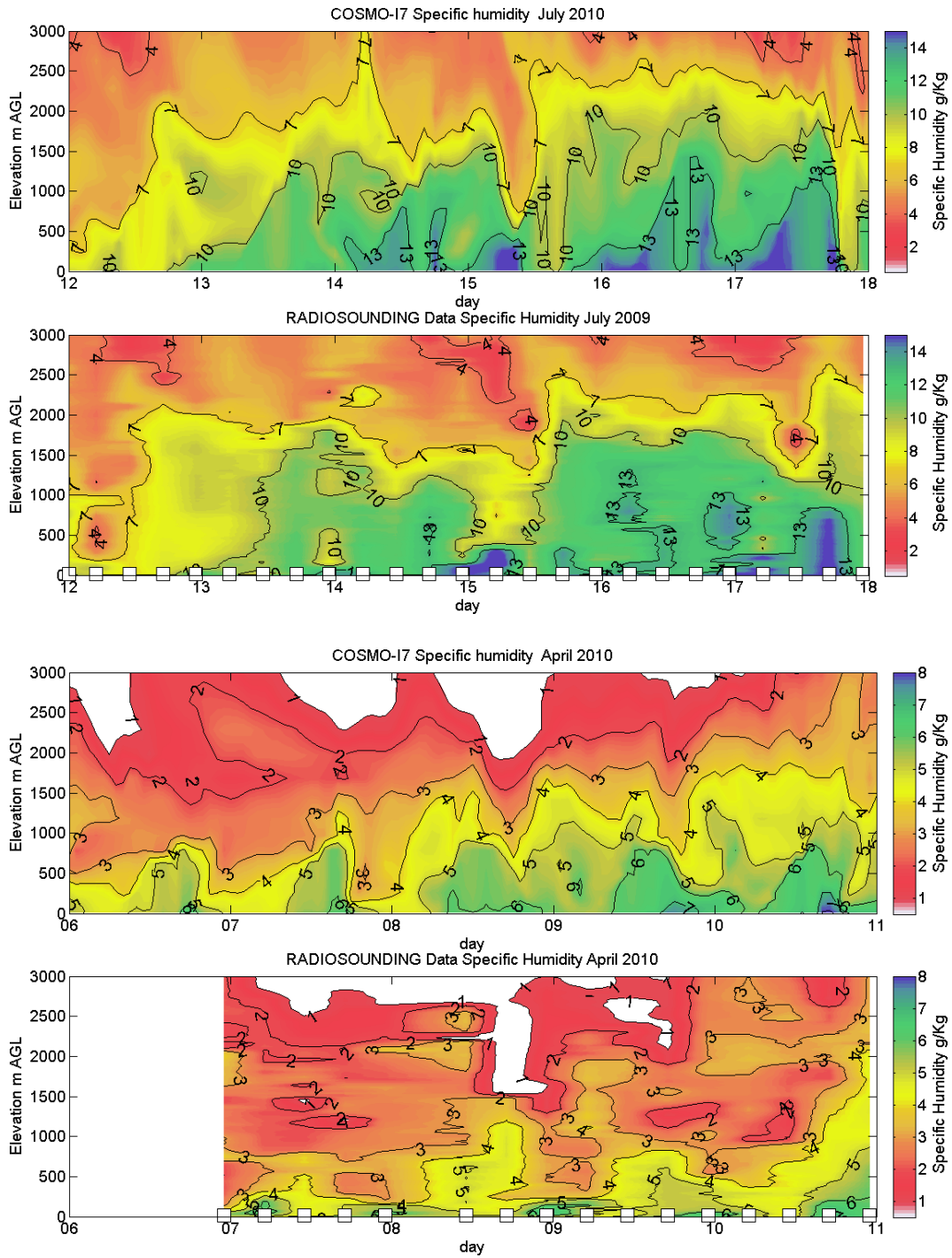


Figure 4.3: As figure 4.2 but for the specific humidity fields.

During the BASE:ALFA campaign the sensible and latent heat fluxes were measured by the LiCor + sonic anemometer through eddy correlation technique and it is, thus, possible to diagnose which of the two hypothesis is correct. Figure 4.4 shows the daily course of the sensible and latent heat fluxes measured and predicted by the COSMO-I7 R-NWP model. Some data gaps are visible due to instrument failures during the summer period which were solved by a complete revamping of the instrument acquisition system. The comparison shows that effectively the latent heat flux is systematically underestimated while the sensible heat flux is systematically overestimated. The problems have thus to be searched in the surface flux estimations from the SVAT modules, and possibly in the time evolution of the ground water and temperature profiles, which can be compared to the observations from the TDR instrument. This simple example shows the importance of having a complete dataset of measurements which allows to separate the contribution to the global error of the various model schemes.

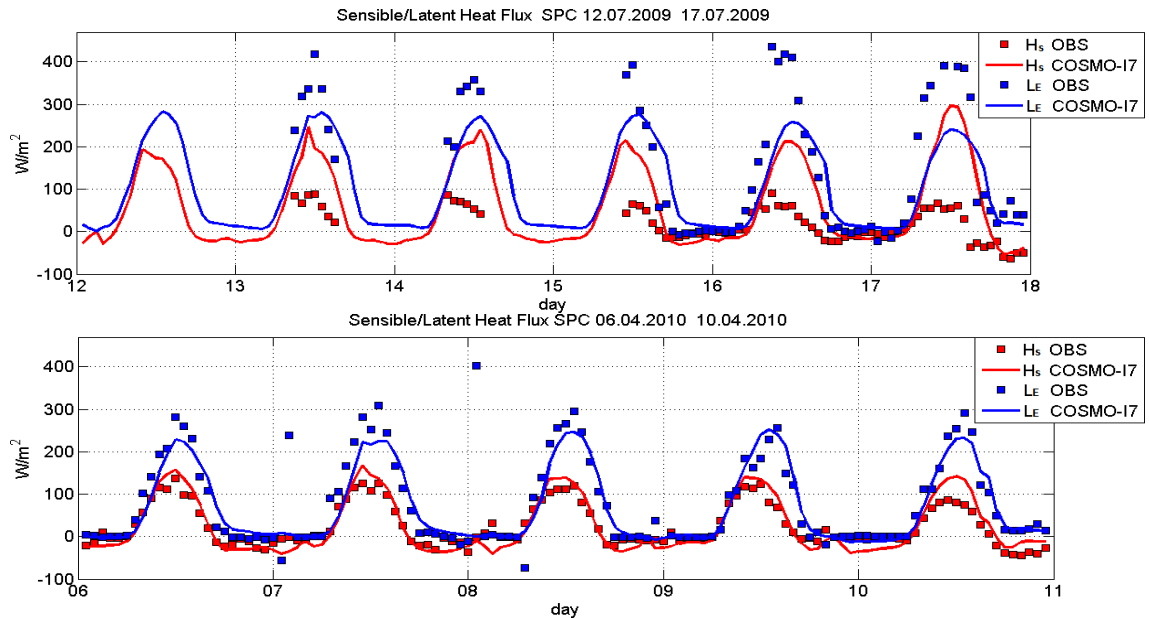


Figure 4.4: Daily course of the sensible (H_s) and latent heat (L_E) fluxes measured and predicted by the COSMO-I7 R-NWP model.

4.2 BLH Comparison

The BL mixing height has been contextually measured by the ceilometer and figure 4.5 presents the LD-40 range-corrected signal (roughly proportional to the aerosol cross section), together with the BLH height retrieved by combination of the WCT and Bayesian analysis [18] during the summer and winter (lower panel) IOPs . As previously mentioned, the daily change in aerosol concentration is driven by both BL evolution and by advection. In this respect, the whole period July 13-17 was affected by an important advection of Saharan dust whose fingerprint is detected by the LD-40 in terms of strong increase in backscatter, both above and within the BL. Therefore, in the summer IOP the presence of elevated layers is rather common, while in spring the aerosol is mostly confined within the BL. It is the presence of elevated layers (either residual or from advectations) that may cause false BL attributions by the LiDAR analysis. In fact, while during the convective phase the aerosol is mostly confined within the BL, when convection weakens, the aerosol does not follow the decrease of the BL height and originates a residual layer. Especially at night, gradient analysis of the LiDAR signal often indicates these layers as the principal ones to classify as H_{mix} . The further Bayesian analysis applied to the data in Figure 4.5 drastically cuts such wrong allocations leading to a very neat inference of BL evolution from the LD-40 data during both advective and non-advective conditions. Because of the non-systematic vertical distribution of the aerosols, both residual or advected layers can also represent a problem in the inference of ground properties from columnar data (such as satellite AOD as discussed in the following section).

Following the methods estimated in the previous section figure 4.6 shows the BLH values calculated from COSMO-I7 outputs with the benchmark estimates from the LiDAR and from radiosondes. The overall agreement among the model estimates of BLH and the determinations derived from radiosoundings and from the LiDAR-Bayesian method is fair, as shown in Fig. 4.6, excluding the TKE method. The first order moments of velocity and temperature (which are used for the Bulk and Gradient Richardson number methods) describe well the diurnal cycle of the boundary layer growth, although some refinement of the coefficient may be made in order to improve the numerical values. The TKE method shows large fluctuations, which often occur in the transition periods, so the estimate cannot be considered robust. In general, it is well known that a closure on the second order moments (like the 2.5 scheme present in COSMO-I7) better performs for the first order

moments, and this can partially justify the variability of the BLH estimates based on TKE with respect to those based on mean velocity and temperature profiles.

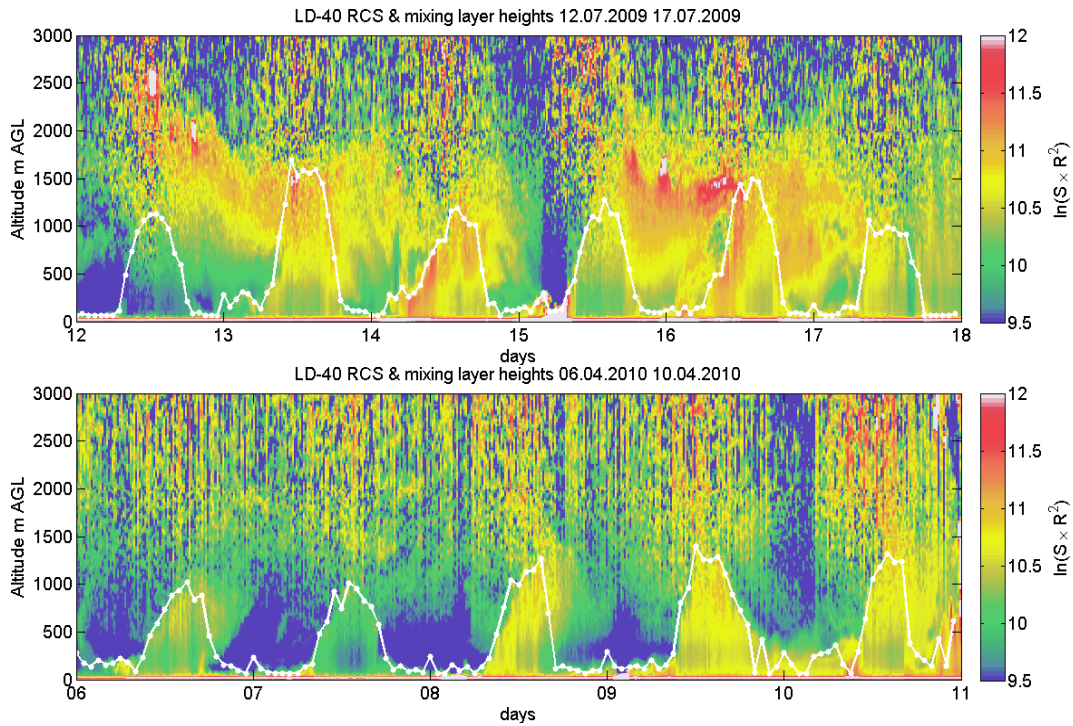


Figure 4.5: Contour plots of the LD-40 measurements made during the summer (upper plot) and spring (lower plot) IOPs. The plots show time and height evolution of both the range-corrected backscatter signal ($\ln \text{RCS}$, colour scale) and of the BL height (white line) over the measuring site. Low (light green) values of $\ln \text{RCS}$ represent a clean atmosphere, while higher values indicate an increasing presence of aerosols. Levels of 12 and above are typically associated with the formation of clouds or fog. The BL height is retrieved from the LD-40 ceilometer data using the WCT analysis 'regularized' by means of the Bayesian method.

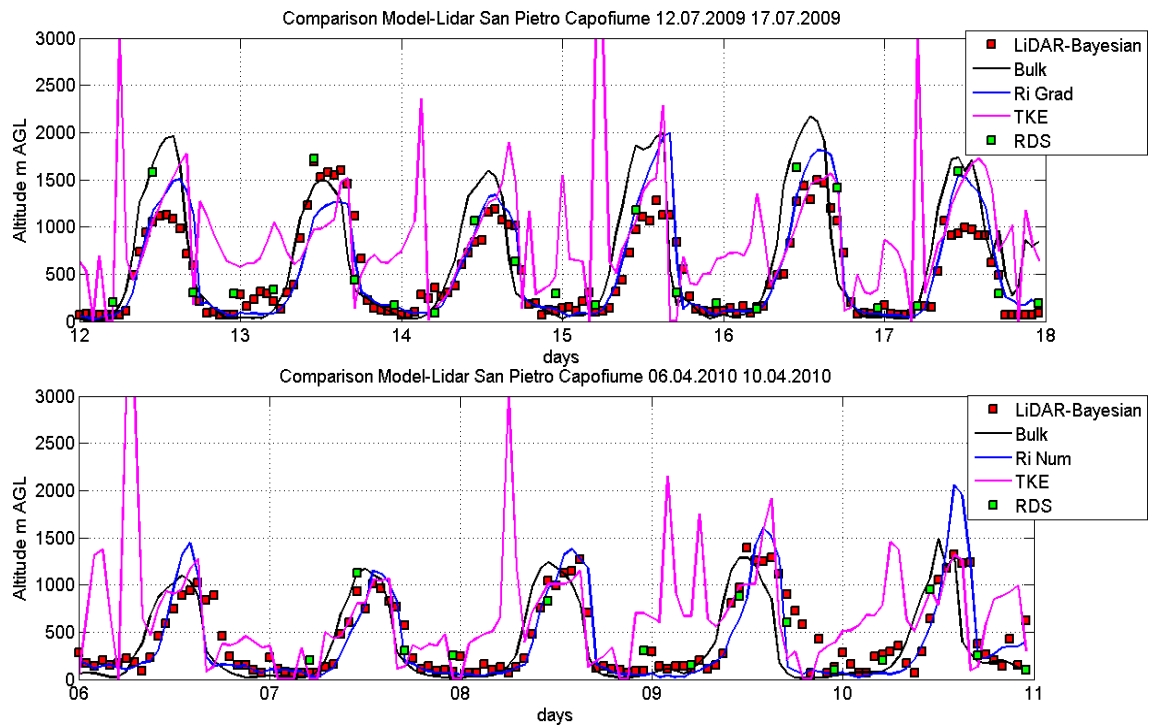


Figure 4.6: Boundary layer height values calculated from COSMO-I7 outputs with the three methods selected and with the benchmark estimates from the LiDAR and the radiosoundings.

4.3 Assessment of pollutant concentration

Pollution is a major threat in urbanized and industrial areas as the Po Valley where elevated PM concentration values are often observed. The continuous measurements of pollutant in the area is therefore an essential part of the monitoring activities of the environmental agencies and the assessment of PM is recognised as key tool to effective pollution management. While in-situ measurement can provide accurate and localized observation, a complete coverage of the territory is intrinsically impossible. Acknowledging this limitation the Directive 2008/50/EC of the European Parliament and of the Council opened the way for alternative methods of pollution assessments by clearly stating that *“Fixed measurements should be mandatory in zones and agglomerations where the long-term objectives for ozone or the assessment thresholds for other pollutants are exceeded. Information from fixed measurements may be supplemented by modelling techniques and/or indicative measurements to enable point data to be interpreted in terms of geographical distribution of concentrations. The use of supplementary techniques of assessment should also allow for reduction of the required minimum number of fixed sampling points”*. The same directive establishes upper limit for daily and annual concentrations of several specie concentrations for effective protection against harmful effects on human health, vegetation and ecosystems.

In this contest PM analysis from air-quality modeling systems and/or estimations derived from satellite products can prove themselves useful tools to overcome discontinuous measurements. They provide a complete coverage of the region even if, admittedly, with lower accuracy, typically depending on resolution and assumptions of the model and/or of the retrieving algorithm. The boundary layer height is a necessary input parameter to obtain a spatial analysis of PM₁₀ concentration whenever a chemical transport model (CTM) or a retrieval technique based on satellite estimates of Aerosol Optical Depth (AOD) is used. Since we showed that BLH definition and therefore numerical value is not unique, the previous estimates will be used in this section to show the range of variability they can produce into PM₁₀ concentration.

The CHIMERE [3] model is selected as CTM. In the ARPA-SIMC operational implementation of CHIMERE, NINFA (“Northern-Italy Network to Forecast Aerosol pollution”), the domain is set to cover the whole Northern Italy to include global scale circulation, which strongly affect the transport and dispersion of pollutants in the Po-Valley [19] (see figure 4.1).

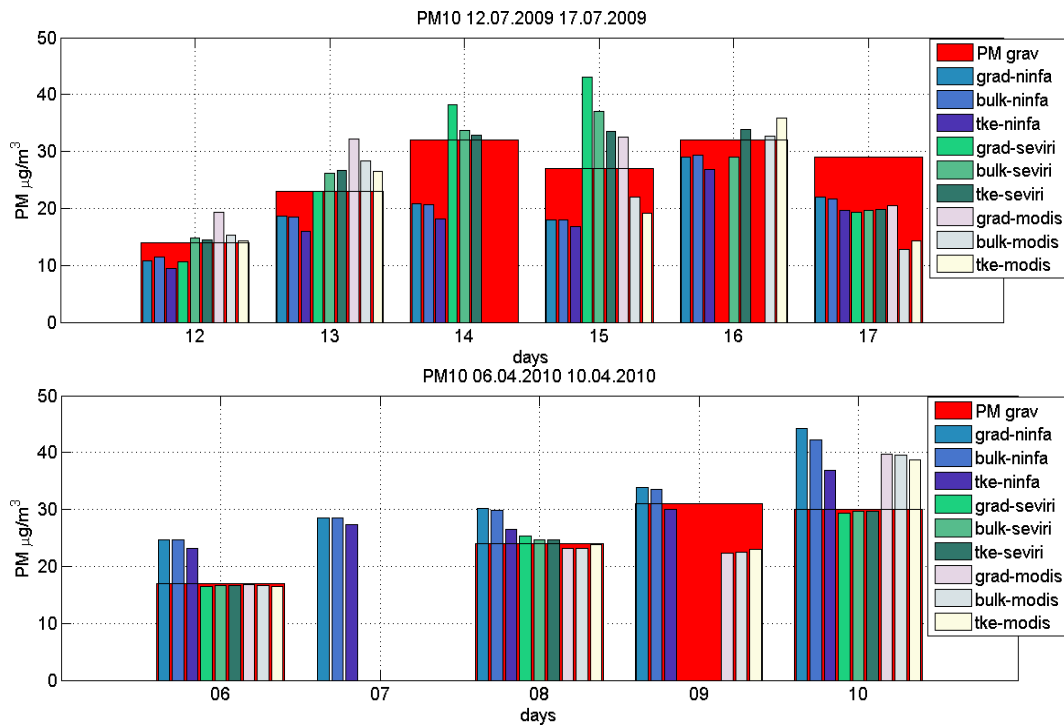


Figure 4.7: Daily mean of PM₁₀ concentration estimated from a chemical-transport model and from retrieval algorithms based on satellite estimates of Aerosol Optical Depth (AOD). The various estimations differ from the assumption used to calculate boundary layer height as discussed in the previous section and are compared to in-situ measurements.

COSMO-I7 provides the meteorological forcing to NINFA, while the PREVAIR ¹ air quality system furnishes hourly concentrations of 23 gaseous and 47 aerosol species at its boundaries. NINFA is routinely used in ARPA-SIMC for daily forecast of Particulate Matter (PM_x), Ozone and NO₂ concentrations and other pollutants. It describes the most important phenomena affecting atmospheric pollutants: emission, diffusion, transport, chemical reactions and depositions following the chemical scheme MELCHIOR of [42] for the gas phase, and it includes an additional module to describe aerosols ². Emission input data are based on the Italian National Inventory of the year 2000 [43].

Similarly to what can be obtained with a chemical transport model, also satellite observations can be usefully employed to derive PM₁₀ estimation at large spatial scales. The idea followed is to use the Aerosol Optical Depth (AOD), which is a measure of the column integrated extinction properties of the atmosphere, properly rescaled to obtain an estimates of the particulate concentration at the ground. [40] suggested that boundary layer height and relative humidity could be used as predictor so that a simple linear relationship relates PM₁₀ to AOD estimations. [22] showed that relative humidity dependence could be omitted over this area so that the relationship between AOD and PM₁₀ reduces to:

$$PM_{10} = \alpha \frac{AOD}{BLH} + \beta \quad (4.1)$$

where the α and β coefficients are calculated using long time series of collocated in-situ PM_{10} observations. Two sets of satellite data are used in this study; the AOD [60] derived from the geostationary Spinning Enhanced Visible and InfraRed Imager (SEVIRI) and the collection 5 standard NASA MOD04 product from the polar-orbiting MODerate resolution Imaging Spectroradiometer (MODIS) [45]. The spatial and temporal resolutions of these aerosol products (10 km and 2 daytime measurements for MODIS, \sim 25 km and observation intervals of 15 minutes for SEVIRI) permit an evaluation of PM estimation from space at different spatial and temporal scales. The calibration coefficients α and β have been calculated using the inverse form

¹ The PREVAIR air quality forecasting system, managed by INERIS, is based on the CHIMERE model on a domain covering most of Europe with a horizontal resolution of 50 km. The two modelling system are therefore rather similar, and can be integrated without inconsistencies. More info on PREVAIR can be found at www.ineris.fr

²model documentation at: <http://euler.lmd.polytechnique.fr/chimere>

of the equation 4.1 considering that AOD estimation errors are larger than the observed PM_{10} error. Moreover the whole BASE:ALFA statistics have been divided in summer and winter periods so that two sets of α and β linear regression coefficients for each of the BLH methods implemented have been used to avoid inconsistencies. Their values are reported in table 4.1 together with the correlation coefficient r of the linear fit.

PM_{10} estimations are compared to in-situ daily mean measurements collected by the air-quality station. It is interesting that the variability in PM_{10} predictions due to a different choice of BLH model is almost always smaller than the distance to the in situ measurements. Even the TKE method which showed unrealistic hourly variation predicts similar concentration to the other two methods, either using CHIMERE, MODIS or SEVIRI retrievals. At least for these conditions the meteorological input provided by the BLH is found less relevant than other factors which can affect the final estimation as for example the pollutant emission. In general both the retrievals and the CTM tend to underestimate the PM_{10} . Only the 15th of July there is a clear over-estimation in the SEVIRI and MODIS retrieved values. From the LiDAR observations in figure 4.5 it is visible that the 12th and 15th of July were characterized by a stratification of aerosol layers above the surface. In these cases the PM_{10} cannot be evaluated using the present approach which implicitly assumes the aerosol well mixed in whole BL and assumptions on the vertical distribution of the particles must be taken into account. Again, as it was shown in the previous section, the presence of the LiDAR in the field enhances the validation procedure by providing several additional information on the aerosols vertical structure and on the BLH development. Once again this simple application shows the importance of having a complete set of measurements for validation purposes.

Table 4.1: Linear regression coefficients for each of the BLH methods implemented together with the correlation coefficient r of the linear fit defined in equation 4.1

BLH Model	SUMMER						WINTER					
	SEVIRI			MODIS			SEVIRI			MODIS		
	r	α	β	r	α	β	r	α	β	r	α	β
Bulk Rich	0.84	97.82	1.83	0.92	136.21	-13.89	1.00	21.04	15.46	0.66	38.98	7.19
Gradient Rich.	0.52	112.81	-4.78	0.66	149.56	-13.92	0.99	23.77	14.86	0.65	48.61	3.24
TKE	0.84	87.02	3.72	0.76	119.30	-13.12	1.00	26.93	15.83	0.68	45.05	10.12

Chapter 5

The Stable Boundary Layer

5.1 Introduction

[73] Stull defines the planetary boundary layer (BL) as the region where air masses are strongly influenced by the surface processes and which interacts through exchange processes with air masses originating from above. Being strongly coupled to the ground, this layer evolution is controlled by turbulence, produced through shear and heat flux, which leads to rapid fluctuations in quantities such as flow velocity, temperature, moisture and to intense vertical mixing.

At the resolution of atmospheric models employed in operational weather forecast, turbulent processes are not explicitly resolved and the Monin-Obukhov similarity theory (MOST) commonly provides the framework for their parameterisation [17, 2]. Accordingly to MOST, temperature and wind profiles below the first model level (in the surface layer) can be diagnosed by scaling prescribed functions with surface turbulent fluxes of heat and momentum. The relationship which holds between mean vertical profiles and surface fluxes is therefore the key element to determine the lower boundary condition for vertical transport in these models.

Using an extensive set of measurements and a multivariate nonlinear regression algorithm [61] it will be shown that in the limit of very stable conditions the Monin-Obukhov similarity theory loses validity. For high atmospheric stability, while it is possible to find values for surface fluxes of momentum and heat to scale the similarity temperature and wind profiles so to match observations, these values are not in agreement with the equiv-

alent measured quantities. In other words surface fluxes are found not to be adequate scaling variables for the mean profiles as they are not sufficient to completely describe the stable boundary layer structure. Discrepancies with the MOST theory become more evident in very stable conditions when the bulk Richardson number (R_b) is larger than $\mathcal{O}(1)$.

5.2 Available dataset

From the RDS profiles, estimates of stable boundary layer (SBL) heights, h_{RDS} , are derived by empirical inspection of the potential temperature profile i.e. subjectively marking the height at which a transition from stable to almost neutral conditions occurs, possibly matching with inflection points of dry temperature, specific humidity and wind speed [18]. This subjective analysis was repeated by three independent people. The standard deviation of the three values for h_{RDS} was smaller than 5% which is then given as an estimate of the h_{RDS} precision.

The surface turbulent fluxes are the other ingredients of the following analysis. They are available at the same location by means of a sonic anemometer which, through the eddy correlation technique, provides sensible and latent heat fluxes, momentum fluxes, CO₂ and H₂O fluxes [35]. The sensor is located at 3.6 m above the ground and fluxes are averaged over 1 h period to reduce measurements uncertainties. The instrument resolution on the flux estimation is particularly critical in this context since in nocturnal BLs the size of the fluxes can be comparable to the instrument sensitivity [10]. Accordingly to the manufacturer specification and consistently with the measurement range set on the sensor these are estimated in $2 \cdot 10^{-3}$ (m²/s²) for the momentum flux and $3 \cdot 10^{-4}$ (K m/s) for the heat flux [71]. During the EBEX-2000 campaign it was found that an important lack of energy balance closure can affect these measurements especially in low wind regimes [58]. This unbalance can be as large as 10% during daytime and it is possibly due to terrain heterogeneity and non-local processes. While we are aware of these limitations it has to be stressed that energy unbalances were found less severe at nighttime when the most of the radiosoundings used in this analysis has been recorded.

5.3 Data analysis

Accordingly to the Monin-Obukhov similarity theory, potential temperature and wind profiles in the surface layer can be diagnosed by scaling prescribed functions with the surface turbulent fluxes. Following the classical formulation [53]:

$$u(z) = \frac{u_*}{\kappa} \left(\log \frac{z}{z_{0,m}} + \Psi_m(\zeta, z_{0,m}) \right) \quad (5.1)$$

$$\theta(z) = \frac{\theta_*}{\kappa} \left(\log \frac{z}{z_{0,h}} + \Psi_h(\zeta, z_{0,h}) \right) \quad (5.2)$$

where

$$u_* = \left(\langle u'w' \rangle^2 + \langle v'w' \rangle^2 \right)^{1/4} \quad (5.3)$$

$$\theta_* = \langle w'\theta' \rangle / u_* \quad (5.4)$$

being u' , v' and w' the turbulent fluctuations in the streamwise, transversal and vertical directions of wind velocity and L the Obukhov length defined as [57]:

$$L = -\frac{\theta_{00}u_*^2}{\kappa g \theta_*} \quad (5.5)$$

Here $\zeta = z/L$, being z the measurement height, θ_{00} is a reference temperature, g is the gravity acceleration, and the von Karman constant κ is equal to 0.4; $z_{0,m}$ and $z_{0,h}$ are the roughness lengths for momentum and heat, respectively.

The Ψ functions, following [2] (see also [48]), are given by:

$$\begin{aligned} \Psi_m(\zeta, \zeta_{0,m}) = & a(\zeta - \zeta_{0,m}) \\ & + b \left[(\zeta - c/d) e^{-d\zeta} - (\zeta_{0,m} - c/d) e^{-d\zeta_{0,m}} \right] \end{aligned} \quad (5.6)$$

$$\begin{aligned} \Psi_h(\zeta, \zeta_1) = & \left(1 + \frac{2}{3} a \zeta \right)^{3/2} + b \left[(\zeta - c/d) e^{-d\zeta} \right] \\ & - \left(1 + \frac{2}{3} a \zeta_1 \right)^{3/2} - b \left[(\zeta_1 - c/d) e^{-d\zeta_1} \right] \end{aligned} \quad (5.7)$$

where $a = 0.7$, $b = 2/3$, $c = 5$, $d = 0.35$, $\zeta_{0,m} = z_{0,m}/L$ and $\zeta_1 = z_1/L$, being z_1 a reference height in the surface layer. They provides a mean profile of the standard log-linear shape for $\zeta < 1$ while for large stability display a complex behavior, to cope with observations. Note that these forms lead to a critical flow Richardson number, but not to a critical bulk Richardson number.

For any of the available radiosounding profiles a multivariate nonlinear regression analysis is performed jointly on the velocity and temperature profiles as defined in equations (5.1) and (5.2). The scaling parameters, u_* and θ_* , are the fitting parameters of the regression and are optimised in an iterative procedure to minimise the mean square distance from the observed radiosounding profiles [61]. The minimisation process is performed using only points below $0.5 h_{RDS}$. This level is on average well above the lowest level of most atmospheric models which is posed between 10 and 20 m considered, in models, the upper limit of the surface layer.

It is therefore less obvious the choice to extend the fit with similarity functions specific for the surface layer up to $0.5 h_{RDS}$. The practical reason is that the regression algorithm needs a statistically significant number of points to reach convergence. An approximate argument can however justify more theoretically this choice. If local similarity holds, than wind and temperature at each height z_i can be expressed in terms of local scaling parameters ($u_*(z_i)$ and $\theta_*(z_i)$ and the local Obukhov length $\Lambda(z_i)$). The dependence of u_* and θ_* on height in stable boundary layers has been studied by [56] and [82]. Both these papers propose slightly different dependences for momentum and heat, but the available data (see for instance the SABLES98 experiment in [13]) do not allow to highlight the difference. Then, we can assume approximately that the functional dependence of u_* and θ_* on the height is the same: $u_*(z)/u_*(z_0) = \theta_*(z)/\theta_*(z_0) = \phi(z/h)$ where we use the same roughness lengths for momentum and heat for simplicity. Accordingly, also the local value of the Obukhov length has the same dependency: $\Lambda(z)/L = \phi(z/h)$. On the other hand, an approximate expression for the similarity profiles for large stability (i.e. for large z/L) is the linear relationship. It is easy to show that, under such conditions, $u(z) \propto u_*(z_0) z/L = u_*(z) z/\Lambda(z)$, and the same holds for temperature. In the present case while we adopted profiles departing from linearity the departure becomes only relevant for large stabilities. Thus the above argument can approximately justify the choice of extending the surface layer relationships up to half of the boundary layer. The initial conditions z_1 and $\theta(z_1)$ needed in equation (5.7) are taken from the lowest point of the radiosounding ascent. A constant roughness length

for momentum, of $z_{0,m} = 11$ cm for the summer profiles, and of $z_{0,m} = 5$ cm for winter profiles is used. These values have been directly derived from the sonic anemometer by means of fitting the logarithmic profile for small stability (i.e. $|z/L| < 0.1$)

Figure 5.1a shows the least-square fit curves superimposed to the radiosounding profiles for a day of example. The boxplots in Fig. 5.1b and 5.1c depict the probability distribution function of the residuals for the whole RDS ensemble. The residuals at height z_i are provided in terms of relative quantities, as $(\text{fit}(z_i) - \text{obs}(z_i)) / (\text{obs}(z_t) - \text{obs}(z_b))$ where $z_t = 0.5 \text{ h}_{RDS}$ and z_b is the ground. They are a measure of how good the regression algorithm is in finding adequate fit parameters to match the observed profiles. Mean residuals for both the wind and temperature profiles are less than 10% when compared to the BL temperature and wind range in the BL. With appropriate scaling parameters the similarity functions in equations (5.1) and (5.2) are therefore able to reproduce the observed data variability. We recall that the fitting (“Predicted”) coefficients are the kinematic momentum and sensible heat fluxes, i.e. $u_{*,P}^2$ and $\langle w'\theta' \rangle_P$. In Figure 5.2 they are compared to the equivalent quantities, $u_{*,S}^2$ and $\langle w'\theta' \rangle_S$, measured by the sonic anemometer, located within the surface layer. It results an overall underestimation of the fluxes predicted by the similarity theory with respect to the measured ones.

It has to be stressed that in some cases $u_{*,P}^2$ and $\langle w'\theta' \rangle_P$ values are below the instrument sensitivity. The inability to adequately measure turbulent fluxes in the nocturnal BL has also been highlighted by [34] and [49] and can exacerbate the discrepancies found in Figure 5.2. Nevertheless these results are reinforced by the fact that the Obukhov length calculated from the mean profiles is smaller than the one obtained from the fluxes recorded by the sonic anemometer (not shown). Therefore it is believed that the boundary layer results more stable if its characterisation is performed via the mean vertical profile than if surface fluxes are used as in atmospheric models.

To better understand the role the atmospheric stability might have in the flux underestimations depicted in Figure 5.2, data have been divided in two categories. The first category collects cases for which there is agreement between the fluxes obtained from the regression and observed ones: this ensemble is defined as the data points for which the momentum or heat fluxes estimated from the fitted parameters are within a factor of three the measured ones (i.e. $u_{*,P}^2 \in [1/3 u_{*,S}^2; 3 u_{*,S}^2]$ and $\langle w'\theta' \rangle_P \in [1/3 \langle w'\theta' \rangle_S; 3 \langle w'\theta' \rangle_S]$). The second category contains all other data, which are considered as ‘outliers’.

The bulk Richardson number at height z_i has been calculated independently for these two categories [68]:

$$R_b(z_i) = \frac{g}{\theta_1} \frac{(\theta_i - \theta_1)(z_i - z_1)}{(u_i - u_1)^2} \quad (5.8)$$

R_b is a measure of the ratio between turbulence inhibition caused by buoyancy and turbulence production due to wind shear. Conceptually, therefore, for each vertical level it provides information on how the eddies production due to surface drag are compensated by the thermal stratification of the atmosphere. The larger R_b the more stable and stratified the atmosphere results to be. For each vertical level the median value of R_b is reported in Figure 5.2(c) for the observed mean profiles. The difference between the two categories is significant. The cases for which there is no agreement between the observed and the fluxes consistent with the similarity theory show an average R_b of 6 with peaks as large as 7 while R_b for the first category is of the order of 1. Clearly the two categories discriminate between stability conditions being the ‘outlier’ profiles markers of very high stability. This result is confirmed also if the observed profiles are substituted with their regression curves (not shown).

The first important finding arising from the analysis in the previous section is that similarity profiles for wind and temperature as from the classic [53] formulation could be used to fit a vast number of radiosounding profiles in diverse stable conditions provided the right scaling is available. Since similarity theory implies that the decay of turbulence with height can be neglected, this result also substantiate the hypothesis that the observed profiles are consistent with a steady turbulence state (although the truth may be different) at least within the accuracy of the observations. Nevertheless, despite similarity profiles for mean quantities can be used to describe the surface layer, turbulent fluxes measured at the surface are not always the right scaling parameters since they are not able to represent the entire variability of the stability. Most strikingly very stable boundary layers are not captured solely by the turbulence measurements. These SBL are characterised by high values of the bulk Richardson number, and by correspondingly high values of the gradient Richardson number, which are both quite larger than the critical values currently used in most atmospheric models [47].

There are important practical consequences of this finding. One is connected to the (in)accuracy of model predictions of boundary layer heights, h , in very stable conditions. As an output of a numerical weather prediction sys-

tem, h can be considered as a diagnostic variable to highlight problems in the energy and momentum exchange between the surface and the atmosphere. Large uncertainties in the estimation of this parameter can be erroneously interpreted as bad forecast capability of BL driven atmospheric phenomena, such as fog, mist or surface triggered convection. From the point of view of chemical transport models, h is also a crucial input parameter characterising the vertical dilution capability of the atmosphere.

In stable BL h is diagnosed mainly relying on surface fluxes as in the [82] formulation:

$$h_{ZE}^{-2} = \frac{f^2}{C_R^2 u_*^2} + \frac{N|f|}{C_{CN}^2 u_*^2} - \frac{|f|(g/\theta_{00})\theta_*}{C_{NS}^2 u_*^3} \quad (5.9)$$

where N is the Brunt-Vaisala frequency of the atmosphere above the SBL top, f the Coriolis parameter and $C_R = 0.6$, $C_{CN} = 1.36$, $C_{NS} = 0.51$ are tuning parameters obtained from a set of large-eddy-simulations (LES) of stable boundary layer conditions which also took into account the influence of the stability of the air above the boundary layer. Figure 5.3(a) shows h_{ZE} and h_{RDS} as a function of z/L which is a measure of the atmospheric stability. h_{RDS} is not uniquely a function of stability and shows large variability for similar z/L values, whereas the diagnostic formulation for h_{ZE} of [82] strongly depends on z/L .

Another example of important practical consequences which stems from the MOST limitations presented here is related to the $2m$ temperature predictions from atmospheric numerical models. θ_{2m} is an important diagnostic variable, Being observed through a vast SYNOP networks, it is used to assess the overall quality of forecasts. The reference measurement height for SYNOP surface observations is in fact $2m$. In models θ_{2m} is a diagnostic variables and is calculated from the ground temperature and the temperature of the first atmospheric level given the stability profiles in the surface layers. Figure 5.3(b) shows therefore that a model with perfect flux predictions (i.e predicted surface fluxes identical to what observed from the sonic anemometer) and with Monin-Obukov similarity theory used as parameterisation of the surface layer, would diagnose $2m$ -temperatures, $\theta_{ref=2m,S}$, which, especially for high stability, are up to $3K$ cooler than what predicted by regressing the similarity functions with mean radiosounding profiles, $\theta_{ref=2m,P}$. From figure 5.3(b) it is clear that $2m$ temperature errors as expected by the application of the MOST in numerical weather prediction systems are not a simple linear function of stability, They have a greater variability. It is

nevertheless clear that as z/L increases toward very stable conditions than surface fluxes do not characterise the entire structure of the BL and for this are not adequate scaling factor for the mean profiles. Non-local processes, such as gravity waves, advection due to horizontal inhomogeneities, and by input of energy from above related to the presence of low level jets are all phenomena which should be taken into account.

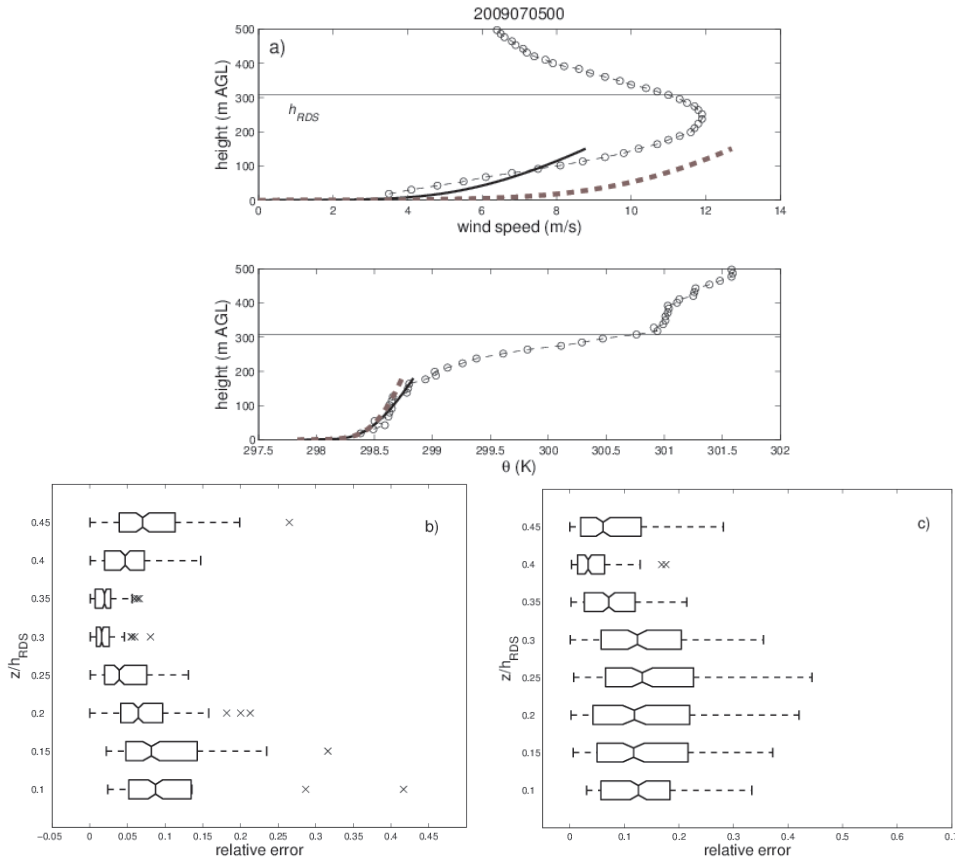


Figure 5.1: Panel a): Wind and potential temperature, (θ), profiles for one of the radiosound ascent at 00UTC of 5th July, 2009, taken as an example. The horizontal lines mark the subjective estimation of BL height, h_{RDS} , for that day. The solid lines are the multivariate regression curves obtained using the Monin-Obukhov similarity theory formulations while the dashes lines are the predictions from eqns (5.1) and (5.2) when the observed surface fluxes are used as scaling parameters. The fit minimises the mean square distance from the observed radiosounding profiles and uses all data points below $0.5 h_{RDS}$. Panel b): Boxplot for the observation residuals expressed in terms of relative errors for the wind speed. On each box, the central line is the median of the distribution, the edges of the box extend from the 25th to the 75th percentile, and the whiskers extend 1.5 times beyond the 25th and 75th percentile. Relative errors outside the whiskers extension are marked with crosses. Panel c): as in Panel b) but for the potential temperature.

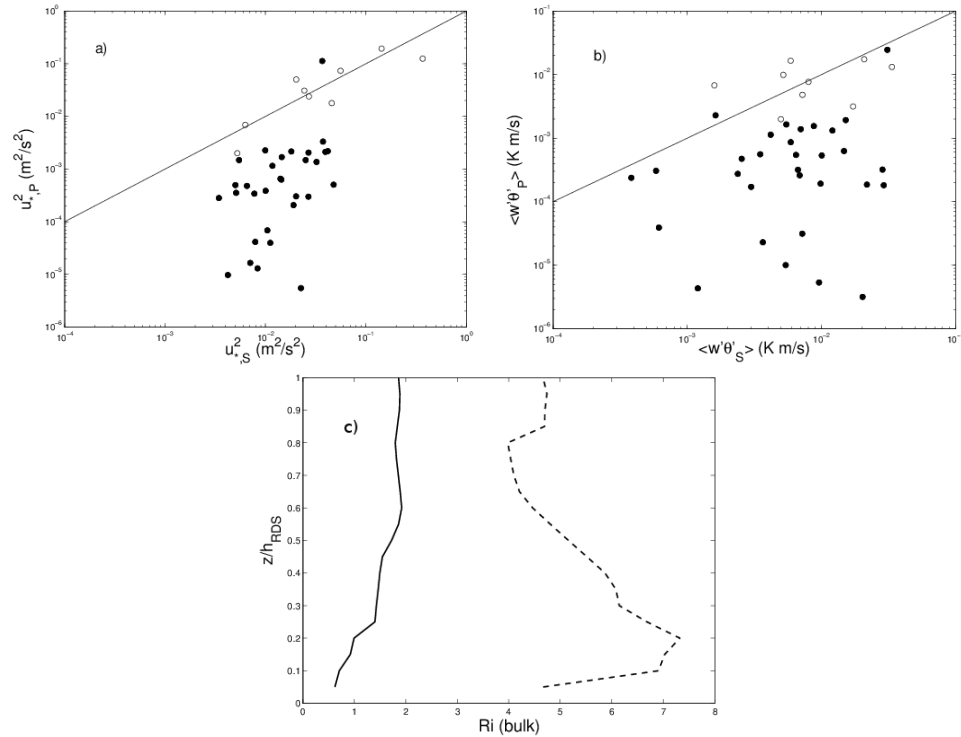


Figure 5.2: Estimated turbulent fluxes from the similarity theory against those measured by the sonic anemometer. Empty circles mark cases for which fluxes estimated by fitting the RDS are in agreement with those measured by the sonic anemometer. Filled circles mark the outliers. Bisectors are indicated by the solid lines. Panel a) flux of momentum, Panel b): flux of heat. Panel c): Vertical profile of the Bulk Richardson number, Rb , calculated for the whole set of RDS profiles. The solid line marks the Rb median profile for which fluxes estimated by fitting RDS profiles agree with those measured with the sonic anemometer. The dashed line is the median profile for outliers.

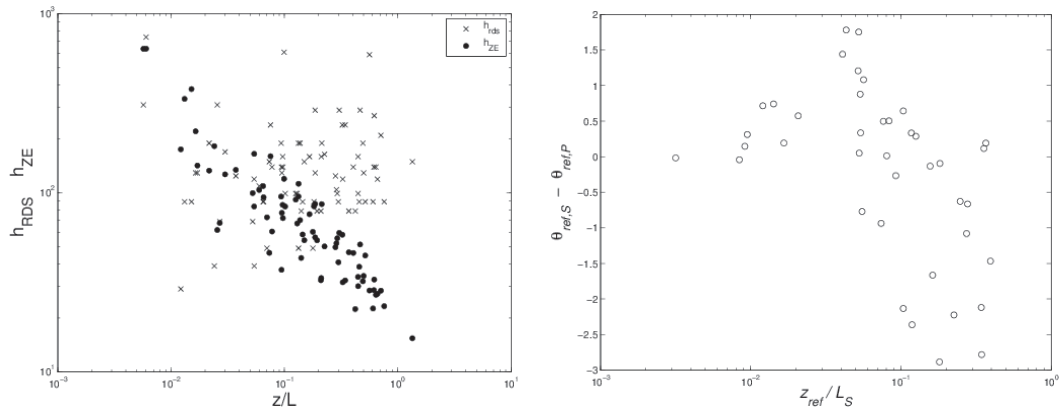


Figure 5.3: Practical consequences of the MOST limitations in stable boundary layers. Panel a): Boundary layer height estimated from subjectively inspecting the RDS profiles, h_{RDS} , and the ones obtained from the diagnostic formulation of [82], h_{ZE} . Panel b): Differences in 2m temperatures as a function of the atmospheric stability. $\theta_{ref,P}$ are diagnosed by scaling the temperature similarity profiles using the “predicted” fluxes from the radiosounding regressions, $\theta_{ref,S}$, using the sonic measured fluxes. L_S is the Obukov length scale calculated from the sonic measurements and $z_{ref}=2\text{m}$.

Chapter 6

Conclusions

This work presents some results on a recent experimental program (BASE:ALFA) which was carried out in the Po-river flatland basin in Northern Italy where the relevant weather regimes are due to the small scale forcing and have for this reason low predictability. Consequently, it has often been noted that forecast performances for the region in boundary layer driven conditions e.g. screen level temperature, fog and low level cloudiness, mixing height, convection triggering, are poor. The project aimed therefore at improving our understanding and the representation of boundary layer processes using observation, physical models and numerical weather prediction parametric schemes. Ceilometers are active instruments which can track the boundary layer depth evolution using aerosols as markers. Their range-corrected signal ($S \times R^2$) is roughly proportional to the aerosol backscatter coefficient. Scanning the $S \times R^2$ in search of discontinuities and applying a threshold to the signal derivative maxima can lead to an automatically detected daily sequence of BL height retrievals, h . In most previous studies the identification of h using only the processing of the ceilometer signal has been performed in a 1D framework, with each vertical column analysed independently. The criterion to select h among all signal discontinuities has been therefore applied statically column-by-column often leading to erroneous estimations which are usually post corrected by the aid of a subjective analysis.

It is evident that an immediate benefit for the retrieval of h would arise from defining a flexible selection criterion which should take into account the dynamical evolution of the whole acquired scene and should allow the identification of stratifications due to physical process in the BL from the ones produced by spurious signals. To fulfil this need the Bayesian Selective

Method (BSM) has been introduced. It was shown, that this new method, in many circumstances is able to “select”, among all the measured stratifications, the one which, in a statistical sense, is the most probable h estimation. The underlying idea of the BSM is to merge information from a preliminary data analysis of the detected ceilometer scene (either conducted with the gradient or the wavelet methods) with what is known on the BL diurnal evolution as predicted by a physical model. The combination is performed in a Bayesian data assimilation framework whose output is a model trajectory which fits in an “optimal” way the data provided. This trajectory is then used to discriminate between realistic and unrealistic ceilometer inflection points or as a proxy of observations where realistic inflection points are not detected.

The comparison against 174 independent BL h estimations from radiosoundings profiles shows the substantial benefit of the BSM approach in comparison to more standard 1D methods for the automated h retrieval from aerosol lidars. A standard data analysis often detects high-level aerosol stratifications which occur during nighttime. These old aerosol layers produce strong signals which are erroneously classified as BL h even if they are not significantly connected to surface processes and should therefore be discarded. The BSM method instead carries information on the low climatological probability to find very large BL heights at night and penalises the selection of these points. Moreover, this new method is able to correctly convey information along the temporal dimension, thus filling gaps in the 1D analysis by taking advantage of the knowledge gained from prior and subsequent detections within the 24 hours assimilation window.

One of the main reasons to design and develop the BSM method was the need of a continuous monitoring of aerosol-based lidar BL heights. Especially under stable conditions when the PBL height determination is still a delicate issue for lidar/ceilometers, the assisted analysis of ceilometer records using the BSM approach presented in this paper provides a possible solution to this problem.

The four months of measurements collected during the BASE:ALFA experiment are being used to investigate processes that govern the exchange of momentum, heat, and mass across the coupled boundary layers. These process studies have involved close collaboration with numerical modelers and many of these investigations are guided by the numerical simulations summarised in table 2.2.

The exercise presented here have been directed toward an air-quality ap-

plication which we found of particular relevance for the Po Valley region which is one of the most polluted areas in Europe. Several models of boundary layer height evolutions have been applied to air-quality forecasting systems and retrieval algorithms.

Nevertheless we did not find that the correct prediction of this parameter always translate in a better estimation of PM_{10} concentrations at the surface. The limited impact of the meteorological forcing on air-quality assessments poses the fundamental problem of trying to improve the modelling of the pollutant emission source and sinks.

Then we focussed our attention on the stable boundary layer. The first important finding arising is that similarity profiles for wind and temperature as from the classic [53] formulation could be used to fit a vast number of radiosounding profiles in diverse stable conditions provided the right scaling is available. Since similarity theory implies that the decay of turbulence with height can be neglected, this result also substantiate the hypothesis that the observed profiles are consistent with a steady turbulence state (although the truth may be different) at least within the accuracy of the observations. Nevertheless, despite similarity profiles for mean quantities can be used to describe the surface layer, turbulent fluxes measured at the surface are not always the right scaling parameters since they are not able to represent the entire variability of the stability. Most strikingly, very stable boundary layers are not captured solely by the turbulence measurements.

There are important practical consequences of this finding. One is connected to the (in)accuracy of model predictions of boundary layer heights, h , in very stable conditions. As an output of a numerical weather prediction system, h can be considered as a diagnostic variable to highlight problems in the energy and momentum exchange between the surface and the atmosphere. Large uncertainties in the estimation of this parameter can be erroneously interpreted as bad forecast capability of BL driven atmospheric phenomena, such as fog, mist or surface triggered convection. From the point of view of chemical transport models, h is also a crucial input parameter characterising the vertical dilution capability of the atmosphere.

Another example of important practical consequences which stems from the MOST limitations presented here is related to the $2m$ temperature predictions from atmospheric numerical models. θ_{2m} is observed through a vast SYNOP network (the reference height for SYNOP surface observations is in fact $2m$). In models θ_{2m} is calculated from the ground temperature and the temperature of the first atmospheric level given the stability profiles

in the surface layers. θ_{2m} is thus an important diagnostic variable. It is nevertheless clear that as z/L increases toward very stable conditions than surface fluxes do not characterise the entire structure of the BL and for this reason they are not adequate scaling factor for the mean profiles. Non-local processes, such as gravity waves, advection due to horizontal inhomogeneities, and by input of energy from above related to the presence of low level jets are all phenomena which should be taken into account.

6.1 Acknowledgements

The BASE:ALFA project was in part financially covered through a fellowship of the Emilia-Romagna Region (Bologna, Italy).

I would like to thank my thesis adviser Prof. Rolando Rizzi for all his support and for giving me the freedom to do my own research. Special thanks to Francesca Di Giuseppe for her patience in explaining different problems and for her willingness to share and discuss various experimental and theoretical issues. Thanks to Stefano Tibaldi, Carlo Cacciamani, Marco Deserti for believing in this program, providing the human resources indispensable for its success. I am thankful for the SIMC group from ARPA-Emilia Romagna, for its nice and fruitful collaboration during BASE:ALFA experiment. A special thanks to Giovanni Bonafé, Angelo Riccio and Francesco Tampieri. I want to thank to the Aerosol Remote sensing Group of Rome (ARS) for their support. Special thanks to the ESSC department and the Boundary layer Group of Reading University. I wish to thank all my friends along the journey, for being along my side during all good and bad times. I would like to thank all the people who have guided and encouraged me during the writing of my thesis. I want to thank my family and in particular to Emilia for understanding and trusting me entirely to fulfill my goals.

Bibliography

- [1] A. Behrendt, S. Pal, F. Aoshima, M. Bender, A. Blyth, Corsmeier U., Cuesta J., G. Dick, M. Dorninger, C. Flamant, et al. Observation of convection initiation processes with a suite of state-of-the-art research instruments during COPS IOP 8b. *Quarterly Journal of the Royal Meteorological Society*, 137:81–100, 2011.
- [2] ACM Beljaars and AAM Holtslag. Flux parameterization over land surfaces for atmospheric models. *Journal of Applied Meteorology*, 30:327–341, 1991.
- [3] B. Bessagnet, A. Hodzic, R. Vautard, M. Beekmann, S. Cheinet, C. Honoré, C. Lioussé, and L. Rouil. Aerosol modeling with chimere—preliminary evaluation at the continental scale. *Atmospheric Environment*, 38(18):2803–2817, 2004.
- [4] A.K. Betts. FIFE atmospheric boundary layer budget methods. *Journal of Geophysical Research*, 97:18523–18531, 1992.
- [5] I. Brooks. Finding boundary layer top: Application of a wavelet covariance transform to lidar backscatter profiles. *Journal of Atmospheric and Oceanic Technology*, 20:1092–1105, 2003.
- [6] F. J. Canny. A Computational Approach to Edge Detection. *IEEE Transactions on Pattern Analysis and Machine Intelligence*, 8(6):679–698, 1986.
- [7] D.J. Carson. The development of a dry inversion-capped convectively unstable boundary layer. *Quarterly Journal of the Royal Meteorological Society*, 99:450–467, 1973.

- [8] S.A. Cohn and W.M. Angevine. Boundary layer height and entrainment zone thickness measured by lidars and wind-profiling radars. *Journal of Applied Meteorology*, 39:1233–1247, 2000.
- [9] S.A. Cohn, S.D. Mayor, C.J. Grund, T.M. Weckwerth, and C. Senff. The lidars in flat terrain (LIFT) experiment. *Bulletin of the American Meteorological Society*, 79(7):1329–1344, 1998.
- [10] D. Contini, A. Donateo, and F. Belosi. Accuracy of measurements of turbulent phenomena in the surface layer with an ultrasonic anemometer. *Journal of Atmospheric and Oceanic Technology*, 23(6):785–801, 2006.
- [11] W.F. Cooke and J.J.N. Wilson. A global black carbon aerosol model. *Journal of Geophysical Research*, 101(D14):19395–19, 1996.
- [12] J. Cuxart, P. Bougeault, and J.L. Redelsperger. A turbulence scheme allowing for mesoscale and large-eddy simulations. *Quarterly Journal of the Royal Meteorological Society*, 126(562):1–30, 2000.
- [13] J. Cuxart, C. Yagüe, G. Morales, E. Terradellas, J. Orbe, J. Calvo, A. Fernández, MR Soler, C. Infante, P. Buenestado, et al. Stable atmospheric boundary-layer experiment in spain (sables 98): a report. *Boundary-Layer Meteorology*, 96(3):337–370, 2000.
- [14] R. Daley. *Atmospheric data analysis*. Cambridge Univ Pr, 1993.
- [15] A. Davis, A. Marshak, R. Cahalan, and W. Wiscombe. The Landsat scale break in stratocumulus as a three-dimensional radiative transfer effect: Implications for cloud remote sensing. *J. Atmos. Sci.*, 54:241–260, 1997.
- [16] K.J. Davis, N. Gamage, C.R. Hagelberg, C. Kiemle, D.H. Lenschow, and P.P. Sullivan. An objective method for deriving atmospheric structure from airborne lidar observations. *Journal of Atmospheric and Oceanic Technology*, 17(11):1455–1468, 2000.
- [17] J.W. Deardorff. Parameterization of the planetary boundary layer for use in general circulation models 1. *Monthly Weather Review*, 100(2):93–106, 1972.

- [18] F. Di Giuseppe, A. Riccio, L. Caporaso, G. Bonafé, G. Paolo, and F.A. Gobbi. Automatic detection of atmospheric boundary layer height using ceilometer backscatter data assisted by a boundary layer model. *Q. J. R. Meteorol. Soc.*, pages 1–18, 2011.
- [19] A. Dosio, S. Galmarini, and G. Graziani. Simulation of the circulation and related photochemical ozone dispersion in the po plains (northern italy): comparison with the observations of a measuring campaign. *Journal of geophysical research*, 107(D22):8189, 2002.
- [20] R.O. Duda and P.E. Hart. *Pattern classification and scene analysis*, volume 1. 1973. pp 482.
- [21] G. Ehret, C. Kiemle, W. Renger, and G. Simmet. Airborne remote sensing of tropospheric water vapor with a near-infrared differential absorption lidar system. *Applied Optics*, 32(24):4534–4551, 1993.
- [22] E. Emili, C. Popp, M. Petitta, M. Riffler, S. Wunderle, and M. Zebisch. PM10 remote sensing from geostationary SEVIRI and polar-orbiting MODIS sensors over the complex terrain of the European Alpine region. *Remote Sensing of Environment*, 2010.
- [23] R. M. Endlich, F. Ludwig, and E. E. Uthe. An automated method for determining the mixing layer depth from lidar observations. *Atmospheric Environment*, 13:1051–1056, 1979.
- [24] I. Faloon, D.H. Lenschow, T. Campos, B. Stevens, M. Van Zanten, B. Blomquist, D. Thornton, A. Bandy, and H. Gerber. Observations of entrainment in eastern Pacific marine stratocumulus using three conserved scalars. *Journal of the Atmospheric Sciences*, 62(9):3268–3285, 2005.
- [25] J. Fiala et al. Spatial assessment of pm10 and ozone concentrations in europe (2005). Technical report, EEA Technical report, 2009.
- [26] C. Flamant, J. Pelon, P. Flamant, and P. Durand. Lidar determination of the entrainment zone thickness at the top of the unstable marine atmospheric boundary layer. *Boundary-Layer Meteorology*, 83:247–284, 1997.

- [27] A. Gelman, J.B. Carlin, H.S. Stern, and D.B. Rubin. *Bayesian Data Analysis*. Chapman and Hall, second edition, 2004. pp 696.
- [28] CSB Grimmond and T.R. Oke. Turbulent heat fluxes in urban areas: Observations and a local-scale urban meteorological parameterization scheme (lumps). *Journal of Applied Meteorology*, 41(7):792–810, 2002.
- [29] J.L. Guerrero-Rascado, M.J. Costa, D. Bortoli, A.M. Silva, H. Lyamani, and L. Alados-Arboledas. Infrared lidar overlap function: an experimental determination. *Optics Express*, 18(19):20350–20359, 2010.
- [30] H. Haario, M. Laine, A. Mira, and E. Saksman. DRAM: Efficient adaptive MCMC. *Statistics and Computing*, 16:339–354, 2006.
- [31] M. Haij, W. Wauben, and H. Klein Baltink. Continuous mixing layer height determination using the LD-40 ceilometer: a feasibility study, 2007. pp. 98.
- [32] B. Hennemuth and A. Lammert. Determination of atmospheric boundary layer height from radiosonde and lidar backscatter. *Boundary-Layer Meteorology*, 120:181–200, 2006.
- [33] C. G. Holzworth. Estimates of mean maximum mixing depths in the contiguous united states. *Monthly Weather Review*, 92:235–242, 1964.
- [34] JF Howell and J. Sun. Surface-layer fluxes in stable conditions. *Boundary-Layer Meteorology*, 90(3):495–520, 1999.
- [35] J.C. Kaimal and J.J. Finnigan. *Atmospheric boundary layer flows: their structure and measurement*. Oxford University Press, USA, 1994.
- [36] R. Kamineni, TN Krishnamurti, R.A. Ferrare, S. Ismail, and E.V. Browell. Impact of high resolution water vapor cross-sectional data on hurricane forecasting. *Geophysical Research Letters*, 30(5):38–1, 2003.
- [37] R. Kamineni, TN Krishnamurti, S. Pattnaik, E.V. Browell, S. Ismail, and R.A. Ferrare. Impact of camex-4 datasets for hurricane forecasts using a global model. *Journal of the Atmospheric Sciences*, 63(1):151–174, 2006.

- [38] C. Kiemle, M. Kästner, and C. Ehret. The Convective Boundary Layer Structure from Lidar and Radiosonde Measurements during the EFEDA'91 Campaign. *Journal of Atmospheric and Oceanic Technology*, 12:771–797, 1995.
- [39] J.D. Klett. Lidar inversion with variable backscatter/extinction ratios. *Applied Optics*, 24(11):1638–1643, 1985.
- [40] RBA Koelemeijer, CD Homan, and J. Matthijsen. Comparison of spatial and temporal variations of aerosol optical thickness and particulate matter over Europe. *Atmospheric Environment*, 40(27):5304–5315, 2006.
- [41] A. Lammert and J. Bösenberg. Determination of the convective boundary-layer height with laser remote sensing. *Boundary-Layer Meteorology*, 119(1):159–170, 2006.
- [42] M. Lattuati. *Impact des émissions européennes sur le bilan d’ozone troposphérique à l’interface de l’Europe et de l’Atlantique Nord: apport de la modélisation lagrangienne et des mesures en altitude*. PhD Thesis, 1997. Université Pierre et Marie Curie, Paris, France.
- [43] R. De Lauretis, A. Caputo, R.D. Córdor, E. Di Cristofaro, A. Gagna, B. Gonella, F. Lena, R. Liburdi, D. Romano, E. Taurino, and M. Vitullo. La disaggregazione a livello provinciale dell’inventario nazionale delle emissioni. Anni 1990-1995-2000- 2005. Technical Report Technical report 92/2009, ISPRA, available at <http://www.sinanet.apat.it/it/documentazione/>, 2009.
- [44] L.Caporaso, A.Riccio, F.Di Giuseppe, and F. Tampieri. The structure of the stable boundary layer as from radiosounding profiles and eddy correlation measurements. *Boundary Layer Meteorology*, pages 1–16, 2012.
- [45] R. C. Levy, L. A. Remer, S. Mattoo, E. F. Vermote, and Y.J. Kaufman. Second-generation operational algorithm: Retrieval of aerosol properties over land from inversion of Moderate Resolution Imaging Spectroradiometer spectral reflectance. *Journal of Geophysical Research*, 112:D13211, 2007.
- [46] A.C. Lorenc. Analysis methods for numerical weather prediction. *Quarterly Journal of the Royal Meteorological Society*, 112:1177–1194, 1986.

- [47] J.F. Louis. A parametric model of vertical eddy fluxes in the atmosphere. *Boundary-Layer Meteorology*, 17(2):187–202, 1979.
- [48] A.K. Luhar, P.J. Hurley, and K.N. Rayner. Modelling near-surface low winds over land under stable conditions: sensitivity tests, flux-gradient relationships, and stability parameters. *Boundary-Layer Meteorology*, 130(2):249–274, 2009.
- [49] L. Mahrt. Stratified atmospheric boundary layers. *Boundary-Layer Meteorology*, 90(3):375–396, 1999.
- [50] G. Martucci, R. Matthey, V. Mitev, and H. Richner. Frequency of Boundary-Layer-Top Fluctuations in Convective and Stable Conditions Using Laser Remote Sensing. *Boundary-Layer Meteorology*, 135(2):313–331, 2010.
- [51] G. Martucci, C. Milroy, and C.D. O’Dowd. Detection of Cloud-Base Height Using Jenoptik CHM15K and Vaisala CL31 Ceilometers. *Journal of Atmospheric and Oceanic Technology*, 27(2):305–318, 2010.
- [52] S. H. Melfi, J. D. Spinhirne, S. H. Chou, and S. P. Palm. Lidar observations of vertically organized convection in the planetary boundary layer over the ocean. *Journal of Climate and Applied Meteorology*, 24:806–821, 1985.
- [53] AS Monin and AM Obukhov. Basic laws of turbulent mixing in the atmosphere near the ground. *Tr. Akad. Nauk SSSR Geofiz. Inst*, 24(151):163–87, 1954.
- [54] Y. Morille, M. Haeffelin, P. Drobinski, and J. Pelon. STRAT: An automated algorithm to retrieve the vertical structure of the atmosphere from single-channel lidar data. *Journal of Atmospheric and Oceanic Technology*, 24:761–775, 2007.
- [55] C. Munkel and J. Rasanen. New optical concept for commercial lidar ceilometers scanning the boundary layer. Technical report, 2004.
- [56] FTM Nieuwstadt. The turbulent structure of the stable, nocturnal boundary layer. *Journal of the atmospheric sciences*, 41(14):2202–2216, 1984.

- [57] AM Obukhov. Turbulence in an atmosphere with a non-uniform temperature. *Boundary-Layer Meteorology*, 2(1):7–29, 1971.
- [58] S.P. Oncley, T. Foken, R. Vogt, W. Kohsiek, H.A.R. DeBruin, C. Bernhofer, A. Christen, E. Gorsel, D. Grantz, C. Feigenwinter, et al. The energy balance experiment ebex-2000. part i: overview and energy balance. *Boundary-Layer Meteorology*, 123(1):1–28, 2007.
- [59] S. Pal, A. Behrendt, and V. Wulfmeyer. Elastic-backscatter-lidar-based characterization of the convective boundary layer and investigation of related statistics. *Ann. Geophys*, 28:825–847, 2010.
- [60] C. Popp, A. Hauser, N. Foppa, and S. Wunderle. Remote sensing of aerosol optical depth over central Europe from MSG-SEVIRI data and accuracy assessment with ground-based AERONET measurements. *Journal of Geophysical Research*, 112:D24S11, 2007.
- [61] WH Press, SA Teukolsky, WT Vetterling, and BP Flannery. *Numerical Recipes 3rd Edition: The Art of Scientific Computing, 2007*. Cambridge Univ. Press, 2007.
- [62] M. Radlach, A. Behrendt, and V. Wulfmeyer. Scanning rotational raman lidar at 355 nm for the measurement of tropospheric temperature fields. *Atmospheric Chemistry and Physics*, 8(2):159–169, 2008.
- [63] B. Ritter and J. F. Geleyn. A comprehensive radiation scheme for numerical weather prediction models with potential applications in climate simulations. *Mon. Wea. Rev.*, 120(2):303–325, 1992.
- [64] L. G. Roberts. *Machine perception of three-dimensional solids*. PhD thesis, Massachusetts Institute of Technology, 1963.
- [65] M.W. Rotach, P. Ambrosetti, F. Ament, C. Appenzeller, M. Arpagaus, H.S. Bauer, A. Behrendt, F. Bouttier, A. Buzzi, M. Corazza, et al. Map d-phase: Real-time demonstration of weather forecast quality in the alpine region. *Bulletin of the American Meteorological Society*, 90:1321, 2009.
- [66] L.M. Russell, D.H. Lenschow, K.K. Laursen, P.B. Krummel, S.T. Siems, A.R. Bandy, D.C. Thornton, and T.S. Bates. Bidirectional mixing in

- an ACE 1 marine boundary layer overlain by a second turbulent layer. *Journal of Geophysical Research*, 103(16):411–16, 1998.
- [67] R. Schrodin and E. Heise. The multi-layer-version of the DWD soil model TERRA/LM. Technical report, Consortium for Small-Scale Modelling (COSMO) Tech. Rep, 2001.
- [68] P. Seibert, F. Beyrich, S.E. Gryning, S. Joffre, A. Rasmussen, and P. Tercier. Review and intercomparison of operational methods for the determination of the mixing height. *Atmospheric environment*, 34(7):1001–1027, 2000.
- [69] J.H. Seinfeld and S.N. Pandis. *Atmospheric chemistry and physics: From air pollution to climate change*. John Wiley New York, 1998. pp 1326.
- [70] P. Skrivanekova. Vaisala radiosonde rs92 validation trial at prague-libus. *Vaisala News*, 164:4–8, 2004.
- [71] R. Sozzi and M. Favaron. Sonic anemometry and thermometry: theoretical basis and data-processing software. *Environmental Software*, 11(4):259–270, 1996.
- [72] J. Steppeler, G. Doms, U. Schättler, H.-W. Bitzer, A. Gassmann, U. Damrath, and Gregoric G. Meso-gamma scale forecasts using the non-hydrostatic model LM. *Meteorol. Atmos. Phys.*, 82:75–96, 2003.
- [73] R. B. Stull. *An introduction to boundary layer meteorology*. Kluwer Academic Publishers, 1988. pp. 666.
- [74] P.P. Sullivan, C.H. Moeng, B. Stevens, D.H. Lenschow, and S.D. Mayor. Structure of the entrainment zone capping the convective atmospheric boundary layer. *Journal of the Atmospheric Sciences*, 55(19):3042–3064, 1998.
- [75] H. Tennekes. A model for the dynamics of the inversion above a convective boundary layer. *Journal of Atmospheric Science*, 30:558–567, 1973.
- [76] M. Tiedtke. A comprehensive mass flux scheme for cumulus parameterization in large-scale models. *Mon. Wea. Rev.*, 117:1779–1800, 1989.

- [77] D.H.P. Vogelesang and A.A.M. Holtslag. Evaluation and model impacts of alternative boundary-layer height formulations. *Boundary-Layer Meteorology*, 81(3):245–269, 1996.
- [78] Q. Wang and D.H. Lenschow. An observational study of the role of penetrating cumulus in a marine stratocumulus-topped boundary layer. *Journal of the Atmospheric Sciences*, 52(16):2778–2787, 1995.
- [79] M. Weissmann and C. Cardinali. Impact of airborne doppler lidar observations on ecmwf forecasts. *Quarterly Journal of the Royal Meteorological Society*, 133(622):107–116, 2007.
- [80] S. Zilitinkevich and A. Baklanov. Calculation of the height of the stable boundary layer in practical applications. *Boundary-Layer Meteorology*, 105(3):389–409, 2002.
- [81] S.S. Zilitinkevich and I.N. Esau. Resistance and heat-transfer laws for stable and neutral planetary boundary layers: Old theory advanced and re-evaluated. *Quarterly Journal of the Royal Meteorological Society*, 131(609):1863–1892, 2005.
- [82] S.S. Zilitinkevich and I.N. Esau. Similarity theory and calculation of turbulent fluxes at the surface for the stably stratified atmospheric boundary layer. *Boundary-Layer Meteorology*, 125(2):193–205, 2007.